

Dynamic view of the solid-state DNP effect

Deniz Sezer

Institute of Physical and Theoretical Chemistry, Goethe University, 60438 Frankfurt am Main, Germany

Correspondence: Deniz Sezer (dzsezer@gmail.com)

Abstract. ~~The first report~~ In the solid effect of dynamic nuclear polarization (DNP) ~~in liquids via the solid-effect mechanism~~ Erb, Motchane and Uebersfeld *Compt. rend.* 246, 2121 (1958) drew attention to the similarity between the field profile of the enhancement and the dispersive component of the EPR line. ~~The implications of this similarity~~ concerted flips of the electronic and nuclear spins, which are needed for polarization transfer, are induced by the microwaves. Commonly, the effect
5 of the microwaves is modeled by a rate process whose rate constant is determined perturbatively. According to quantum mechanics, however, ~~were not pursued subsequently as practically at the same time~~ Abragam explained the effect in terms of state mixing by the dipolar interaction. Here we develop a description of the solid effect which is grounded in the dynamics of the electron-nucleus spin system, rather than the static view of state mixing. ~~Our approach~~ coherent microwave excitation leads to Rabi nutation, which corresponds to a rotation rather than a rate process. Here we reconcile the coherent effect of the
10 microwaves with the description by rate equations by focusing only on the steady state. We show that the phenomenological rate constants describing the synchronous excitation of the electronic and nuclear spins can be selected such that the description by rate equations yields the same steady state as the exact quantum mechanical treatment. The resulting non-perturbative rates differ from the classical, perturbative ones and apply also at the high microwave powers used in DNP. Our non-perturbative treatment of the solid effect highlights the role of the coherences in the mechanistic steps of polarization transfer, and ~~shows~~
15 ~~that the offset-dependence of the DNP enhancement can be rationalized as the response of two band-pass filters connected in series. The first filter is the power-broadened EPR line; the second filter consists of two parts centered on both sides of the electronic resonance and displaced by one nuclear Larmor frequency from it. Being proportional to the product of the two filters, the DNP enhancement profile acquires its odd symmetry from~~ reveals the importance of the dispersive component of the EPR line. Interestingly, the multiplicative dependence of the DNP enhancement on the dispersive EPR line ~~, as intuited~~
20 ~~by Erbet al. and in agreement with their phenomenological treatment. The developed~~ was intuited in the very first report of the solid effect in liquids [Erb, Motchane and Uebersfeld *Compt. rend.* 246, 2121 (1958)]. The time-domain description of the solid effect developed here is extendable to liquids, where the dipolar interaction changes randomly in time due to molecular diffusion.

1 Introduction

25 The ~~issue of~~ *Comptes rendus* from April 9, 1958, contained the article “Effect of nuclear polarization in liquids and gases adsorbed on charcoal” by Erb, Motchane and Uebersfeld (Erb et al., 1958a). It reported enhancements of the proton-NMR

30 signal of benzene upon microwave (mw) irradiation of the EPR line of charcoal. The enhancements were positive at fields larger than the EPR resonance position and negative at smaller fields. Because fields symmetrically displaced from the resonance yielded the same magnification factor, the enhancement profile was odd in the field offset and resembled the dispersive component of the EPR line. The similarity between the two prompted the authors to augment the Solomon equation (Solomon, 1955) with two new terms proportional to s_x and s_y (Erb et al., 1958a):

$$\dot{i}_z = \lambda(i_z - i_z^{\text{eq}}) + \mu(s_z - s_z^{\text{eq}}) + \nu s_x + \rho s_y.$$

35 Here $i_z = \langle I_z \rangle$ and $s_n = \langle S_n \rangle$ ($n = x, y, z$) are the expectation values of the corresponding spin operators, i_z^{eq} and s_z^{eq} are the nuclear and electronic polarizations at equilibrium, and the dot above i_z indicates differentiation with respect to time. Taking into account that “under saturation conditions $s_y = 0$ ” the authors arrived at

$$\dot{i}_z = \lambda(i_z - i_z^{\text{eq}}) + \mu(s_z - s_z^{\text{eq}}) + \nu s_x.$$

Assuming μ was small in their case, they solved at steady state as

$$i_z^{\text{ss}} = i_z^{\text{eq}} - (\nu/\lambda)s_x^{\text{ss}},$$

40 which explained the similarity between the field profile of the enhancement and the dispersive EPR line. Boltzmann polarization of electronic spins in a magnetic field is orders of magnitude larger than that of nuclear spins. When the electronic and nuclear spins interact with each other, it becomes possible to transfer the much larger polarization of the former to the latter. Such transfer, known as dynamic nuclear polarization (DNP), can be achieved in several ways, which differ in their mechanistic steps. Two of the DNP mechanisms, namely the Overhauser effect and the solid effect, can be explained by considering a minimal system comprising one electronic spin and one nuclear spin. To explain the other two DNP mechanisms known as
45 the cross effect and thermal mixing, it is necessary to consider one nuclear spin interacting with, respectively, two and many coupled electronic spins (Wenckebach, 2016). The current paper engages only with the former two DNP mechanisms.

The next installment of *Comptes rendus* from April 14, 1958, contained Abragam and Proctor’s report “A new method for dynamic polarization of atomic nuclei in solids” (Abragam and Proctor, 1958), which was printed 132 pages after Erb et al. (1958a). This seminal contribution provided the theoretical understanding, and subsequently also the name, of the solid-state effect of
50 dynamic nuclear polarization (DNP). In particular, Historically, the Overhauser effect was the authors argued that the excitation of the forbidden transitions $(++) \rightleftharpoons (--)$ and $(+-) \rightleftharpoons (-+)$, which become weakly allowed because the dipolar coupling yields mixed states of the form $(--) + q(-+)$, could be used for DNP. (\pm first to be conceived (Overhauser, 1953) and observed experimentally, initially in metals and subsequently also in liquids (Carver and Slichter, 1953, 1956). A rigorous theoretical understanding of the effect in nonmetals was provided shortly after the first experiments (Abragam, 1955; Solomon, 1955).
55 At the core of this understanding are the states of the two spin types, both taken as 1/2 for simplicity.) As an experimental verification of the theoretical proposal, the Boltzmann polarization of ^{19}F nuclei was used to enhance the NMR signal of ^6Li in a LiF monocrystal, thus demonstrating polarization transfer from nuclei with larger to nuclei with smaller gyromagnetic ratios (i.e., a *nuclear solid effect*). Solomon equations, which describe the relaxation processes in a system of two interacting spins (Solomon, 1955).

60 The parameter of mixing of the Zeeman energy levels, obtained from first-order perturbation theory under the assumption that the dipole-dipole interaction with the electron is much smaller than the nuclear splitting (Abragam, 1955) is

$$q = \frac{1}{4} \frac{D_{\text{dip}}}{\omega_I} \frac{-3 \cos \theta \sin \theta e^{i\phi}}{r^3}.$$

Here ω_I is the nuclear Larmor frequency, $D_{\text{dip}} = (\mu_0/4\pi)\hbar\gamma_S\gamma_I$ is the dipolar constant, and (r, θ, ϕ) are the spherical polar coordinates of the relative position vector of the spins. The probability amplitude to excite a zero-quantum (ZQ) or double-quantum (DQ) transition between the mixed energy levels is then proportional to $\omega_I q$, where ω_I is the mw nutation frequency. Combining the probability of excitation with the Lorentzian spread of the electronic energy levels, as reflected by the homogeneous width of the EPR line, one arrives at the rates of the ZQ and DQ transitions (Wind et al., 1985):

$$v_{0,2}(\Omega) = 4(q^* q) v_1(\Omega \pm \omega_I)$$

(the upper sign belongs to v_0 and the lower to v_2), where

70
$$v_1(\Omega) = \frac{1}{2} \omega_I^2 \frac{R_{2S}}{R_{2S}^2 + \Omega^2}$$

is the rate of the allowed (single-quantum) EPR transition. In these expressions, $\Omega = \omega_S - \omega$ is the offset of the mw frequency ω from the electronic resonance frequency ω_S , and R_{2S} is the electronic T_2 relaxation rate. In essence, the rates of the forbidden transitions are obtained by shifting the rate of the allowed transition by $\pm\omega_I$ along the frequency axis and multiplying by $4|q|^2$. For our purposes, it is useful to discern two aspects of the theoretical formalism. On the one hand, the evolution of the electronic and nuclear polarizations is described by two coupled differential equations (Solomon, 1955, eq. 14), analogous to the rate equations of chemical kinetics. On the other, the phenomenological rate constants that appear in these rate equations are expressed in terms of the quantum-mechanical probabilities for transition between two distinct energy states (Solomon, 1955, eq. 15). To first order in a perturbative calculation, the amplitude of such transition probabilities per unit time is proportional to the matrix element of the relevant interaction term in the spin Hamiltonian (Solomon, 1955, eq. 3). While the name Solomon equations is mainly used to refer to the first of these aspects (Keeler, 2010), the perturbative calculation of the transition probabilities per unit time is an integral part of the theoretical description. In fact, the idea that interaction terms in the Hamiltonian have corresponding probabilities per unit time to induce transitions (i.e., what we have called the second aspect of the theory), provides the logical justification for the description by rate equations (Abragam, 1955; Solomon, 1955; Webb, 1961).

85 ~~One month and a half after Abragam and Proctor's report~~ The solid-state effect (or solid effect) was the second DNP effect that was observed experimentally and explained theoretically (Abragam and Proctor, 1958). In the Overhauser effect, the simultaneous flips of the electronic and nuclear spins, which are needed to couple the electronic and nuclear polarizations, are achieved by thermal relaxation; in the solid effect, these synchronous spin flips are driven coherently by the microwave irradiation. Thus, in the May 28, 1958 issue of *Comptes rendus*, Erb, Motehane and Uebbersfeld published another report with the lengthy title "On a new method of nuclear polarization in fluids adsorbed on charcoal. Extension to solids and

in particular to irradiated organic substances” (Erb et al., 1958b). There, the authors state (our translation) The experiments Erb et al. (1958a) had been carried out with charcoal whose half-linewidth was 5 gauss and the multiplication factor seemed to reproduce the paramagnetic dispersion curve.

The new experiments indicated that the increase in polarization of the proton in the adsorbed fluid is maximum in all cases,
95 when the solid effect, the phenomenological rate constants of the rate equations are calculated from the matrix elements of the microwave term in the Hamiltonian. For this term to excite nuclear spin flips, the dipolar interaction between the electronic and nuclear frequencies are chosen such that the nuclear resonance field differs from the electron resonance field $\delta H = \pm 5$ gauss (within 10%) spins should mix the Zeeman energy states, and thus make the zero-quantum (ZQ) and double-quantum (DQ) transitions weakly allowed (Abragam and Proctor, 1958).

100 ~~These results support the suggestion of Abragam that the new theory of Abragam and Proctor on the nuclear polarization in solids (Abragam and Proctor, 1958) must apply to these new phenomena, and invalidates the interpretation proposed previously (Erb et al., 1958a).~~

The value of 5 gauss found in the case of the proton indeed corresponds to the value deduced from the theoretical formula $H_0 \pm \delta H = (\omega \pm \omega_N) / \gamma_e$.

105 This seems to have sealed the fate of the insightful observation of Erb, Motchane, and Uebbersfeld (Erb et al., 1958a) that the odd parity of the solid-effect DNP field profile resembles the dispersive component of the EPR line. In the mean time, Abragam’s explanation of the solid-state effect in terms of level mixing has become deeply embedded in Although the Overhauser effect and the thinking of the modern-day DNP researcher, whose quantitative analysis of the experimental data starts with the mixing parameter q (Wind et al., 1985).

110 ~~In this paper we demonstrate that eq. is correct. We show that the DNP field profile is odd in the field offset for the same reason that solid effect are described using a consistent theoretical formalism (with its two complementary aspects explained above), quantum-mechanically there is a major difference between relaxation and coherent excitation. By their very nature, the rate equations of the polarizations model all evolution as exponential decay/increase towards some steady state. However, according to quantum mechanics, the dispersive component of the EPR line is odd, as intuited by Erb, Motchane and Uebbersfeld (Erb et al., 1958a). In fact, one could justifiably say that s_x and s_y are indeed responsible for the solid effect, exactly as described in . The contribution of s_y does become negligible at lower mw powers or higher magnetic fields effect of the microwave field is to rotate the magnetization, leading to the phenomenon known as Rabi nutation. Since rotation and exponential decay/increase are fundamentally different, modeling the effect of the microwaves as a relaxation process should not be possible in general. This raises questions about the fundamental applicability of the first aspect of our theoretical understanding, namely the rate-equation formalism, to the description of the coherently-driven polarization transfer in the solid effect (as opposed to the relaxation-driven transfer in the Overhauser effect). Because the rate equations are justified by the idea that interaction terms induce transitions with a constant probability per unit time, the possibility to model the effect of the microwaves through a perturbative rate constant also becomes questionable. It should be pointed out that these concerns are not new. Indeed, in the case of single spin 1/2, where the solid effect is solely due to the dispersive component, in agreement~~
125 with quantum dynamics is described exactly by the Bloch equations, Abragam explicitly analyzes how the rate equation with a

perturbative rate constant for the microwave (mw) excitation relates to the exact solution, both at short times and at long times (Abragam, 1961, pp. 27-32).

~~To arrive at these results we depart from the static picture of~~ While many modern applications of DNP in the solid state rely on pulsed methods (Can et al., 2015; Quan et al., 2022), here we consider only continuous-wave (cw) excitation, where
130 one is exclusively interested in the steady state of the spin dynamics. As a result, we will be only concerned with how the description of the solid effect, in which the ratio of the dipolar and nuclear Zeeman interaction energies serves as a perturbation parameter (eq.). In this approach the rates of the forbidden transitions acquire a factor of ω_T^{-2} from $|q|^2$, and a factor of ω_T^2 from the mw excitation (eq. by rate equations relates to its proper quantum-mechanical description at steady state. To this end, in Sec.), without any room for non-trivial cross-talk between these two frequencies. Such cross-talk is also not provided by the
135 Lorentzian dependence on Ω we examine the two descriptions for a single spin 1/2 and, following Abragam (1961), confirm that the perturbative rate constant of mw excitation leads to the same steady state as the Bloch equations.

~~Instead,~~ Motivated by this observation, in Sec. 3 we adopt the same perspective to analyze the system composed of one electronic and one nuclear spin 1/2. In this case, starting with the Liouville-von Neumann equation of the density matrix, we
140 obtain first derive proper quantum-mechanical equations of motion for the expectation values of the spin operators that are relevant to the solid effect. We identify the rates of the forbidden transitions by analyzing the ~~Then we show that one can analytically solve for the~~ steady state of these dynamical equations. The resulting analytical expressions are exact, and like the classical expressions (eq.) contain the squares of the dipolar interaction and of ω_T as multiplicative factors. Their offset dependence, however, couples ω_T and ω_I in a non-trivial way, which reduces to the classical expressions when $\omega_T \ll \omega_I$ but predicts qualitatively different dependence when ω_T is similar to or larger than ω_I . Given the large mw powers currently used
145 in DNP, $\omega_T \approx \omega_I$ should hold at X-band (Neudert et al., 2016) and to a lesser degree at Q-band.

~~The main visual understanding that arises from our dynamical analysis can be summarized as follows. In the solid effect, the transfer of polarization from the electron to~~ the exact quantum dynamics, under the simplifying assumption that the dynamics of the electronic spins is not affected by the hyperfine interaction with the nuclei. Since, at steady state, all coherences can be expressed in terms of the nucleus is mediated by several coherences of two different types: (i) purely electronic and (ii)
150 containing both the electronic and nuclear spin operators. The former act as a Lorentzian band-pass filter centered at the electronic Larmor frequency; the latter as two (approximately) Lorentzian band-pass filters centered at $\omega \approx \omega_S \pm \omega_T$. These filters are depicted in fig. 10, which shows only half of the second filter for clarity. The polarization transfer efficiency depends on the overlap (i.e., product) of the two filters since they are connected in series ~~polarizations, it becomes possible to rewrite the dynamical equations in terms of the polarizations only. Comparing the resulting equations with the rate equations of the~~
155 polarizations, we select the phenomenological rate constants that appear in the latter, such that the two descriptions have identical steady states.

~~Two band-pass filters centered at ω_S (blue) and $\omega_S \pm \omega_T$ (red). The solid effect efficiency is proportional to the product of the even (with respect to ω_S) component of one of the filters and the odd component of the other filter, since the two filters are connected in series. Increasing the mw power (ω_I) increases the intensities of both filters, thus their product grows~~
160 quadratically. Increasing the magnetic field (ω_T) decreases the intensity of the second filter and shifts it to the right, thus

quadratically decreasing the overlap with the first filter. The second filter has another symmetrical component centered at $\omega_S - \omega_I$ which is not shown. Stated differently, we abolish the idea of constant transition probabilities per unit time as justification for the rate equations. Instead, we view the rate equations as a convenient mnemonic for encoding the steady state of the exact quantum dynamics, thus providing a shortcut to the analysis of this steady state. Having decoupled the phenomenological rate constants from the perturbative calculation of the mw-induced transition probabilities, we are free to select them such that the mnemonic yields the correct steady state. We find that the rate constants for the ZQ and DQ transitions selected in this way differ from the corresponding perturbative rate constants that are currently used in the literature (Abragam and Goldman, 1978; Wind et al., 1985; Duijvestijn et al., 1986).

The classical expression for the forbidden transition rates (eqs. In Sec. and) accounts only for the even part of the second filter (solid red line in fig. 10). According to our picture, this even component has to be multiplied by the imaginary (odd) part of the first filter (dashed blue line) which is nothing but the dispersive EPR line that Erb, Motehane and Uebbersfeld suspected to play a central role in the solid effect. At the canonical offset of the solid effect, $\omega_S + \omega_I$, this corresponds to the product of the blue and red filled circles in fig. 10. 6 we show that our new rate constants reproduce the classical expressions when the Rabi nutation frequency ω_1 is much smaller than the nuclear Larmor frequency ω_I , as required by the perturbative treatment. Our new analytical expressions for driving the forbidden transitions, however, also hold when $\omega_1 > \omega_I$, as could happen at S and X bands, given the high microwave powers currently employed in DNP experiments with resonance structure (Neudert et al., 2016; Denysenkov et al., 2022). These new expressions are the main analytical result of the current paper.

Since multiplication is commutative, in this mental picture there is an apparent duality between the two types of filters. The colored circles in fig. 10 are at the maximum of the even part of the red filter, which is multiplied by the odd part of the blue filter. But for the solid effect one also multiplies the odd part of the red filter with the even part of the blue filter. At the maximum of the latter (blue diamond) the odd part of the red filter equals zero (red diamond). As a result, the solid effect is observed at $\omega_S \pm \omega_I$ but not at ω_S .

The amplitudes of the solid red line and dashed blue line increase linearly with ω_I , hence their overlap at $\omega_S + \omega_I$ scales with ω_I^2 . The amplitude A complete description of the spin dynamics of the four-level system that we analyze here requires only 16 different spin operators, including the identity operator. The dynamics is thus encoded by a 16×16 propagation matrix in Liouville space, and can be simulated numerically using a spin-dynamics simulation package (Bengs and Levitt, 2018; Yang et al., 2022). Such numerical simulations are currently often employed to explore the efficiency of the solid red line decreases linearly with ω_I . Since ω_I also changes the distance of this filter from the electronic filter, the overlap at $\omega_S + \omega_I$ scales inversely with ω_I^2 . This is how the factor ω_I^2/ω_T^2 , which in the classical description resulted from substituting and into , arises in our picture.

The theoretical justification and details of this alternative description of the solid effect are presented in the following sections. We start with an overview of the rate equations of the electronic and nuclear polarizations, and connect their steady state to effect for various experimental parameters. However, even in the relatively simple case of a four-level system, observing a certain effect in the DNP enhancement (Sec. ??). The focus here is on the phenomenological rate constants used to describe the forbidden transitions. After that , in Sec. 4, we derive quantum-mechanical equations of motion for the spin operators of relevance to the solid effect. In simulations does not automatically provide understanding about the mechanism of this effect.

as demonstrated recently by Quan et al. (2023), who strive to explain the origin of a dispersive DNP component seen both in experiments (Shankar Palani et al., 2023) and in their numerical simulations. Clearly, developing intuition about the spin dynamics that is relevant for a given phenomenon is invaluable.

200 The general quantum dynamics of a four-level system can be described through 15 coupled differential equations for the expectation values of the 15 spin operators, excluding the identity. The equations that we derive in Sec. ?? we require that these equations of motion and the rate equations of 3.1, together with the Bloch equations from Sec. ?? have identical steady states. This allows us to express the phenomenological rate constants in terms of the parameters of the problem. In Sec. ?? we examine the relationship between the classical expression of the forbidden transition rates (eq.) and our results. Our conclusions are given 2.2, constitute seven such equations. (In fact, we implicitly account for three more operators, thus covering ten out of 205 the 15 possible ones, as explained in Sec. 7.3.4.) When the number of coupled differential equations increases beyond three, gaining an intuitive insight into the dynamics that they describe becomes difficult.

Differently from the static picture based on level mixing and perturbation theory, the dynamical description developed here is readily extendable to liquids (Erb et al., 1958a; Leblond et al., 1971; Gizatullin et al., 2022; Kuzhelev et al., 2022) where the dipolar interaction is time-dependent. Such extension is presented in the companion paper (Paper II). There we show that 210 the random molecular motions in liquids broaden the second filter in fig. Inspired by the graphical representation of chemical reactions in biochemistry, in Sec. 40, thus decreasing its amplitude at $\omega_S + \omega_T$. This substantially reduces the product at the position of the red and blue filled circles, and hence the efficiency of 4 we represent visually the coupled differential equations describing the solid-effect spin dynamics. The resulting “flow diagram” sheds light on the dynamical interconnections between the spin polarizations and the coherences that are active in the solid effect. At the same time, however, the motional broadening increases the tail of the solid red line at the location where the dispersive EPR component (dashed blue line) has a maximum. As a result, the product of the two amplitudes at the positions of the blue and red stars in fig. In Sec. 10 may become sufficiently large to be manifested in the DNP field profile. One then sees solid-effect enhancements at “wrong” offsets, in addition to the enhancements at the “correct” solid-effect offsets (Kuzhelev et al., 2022). Under such conditions, the dispersive component of 5 we study the algebraic relationships between the coherences and the polarizations that emerge at steady state. When 220 considered in the context of the dynamical interconnections, these algebraic relationships highlight the importance of the purely electronic coherences in the EPR line is manifested in the solid-effect DNP field profile, visually confirming the hunch of Erb, Motehane and Uebbersfeld (Erb et al., 1958a). transfer of polarization, with the out-of-phase (i.e., dispersive) component playing a prominent role. Interestingly, the importance of the dispersive EPR line for the solid effect was intuited already in the first report of the solid effect in liquids (Erb et al., 1958a), as we discuss in Sec. 7.2. Our conclusions are presented in Sec. 225 7.3.

2 Allowed EPR transition

3 **Rate equations**

In the rate-equation treatment of DNP (Abragam, 1955; Webb, 1961; Barker, 1962) the Overhauser and solid effects (Webb, 1961; Barker, both thermal relaxation and mw excitation are envisioned as randomly flipping spins between pairs of energy levels with certain
230 rates, as depicted in figs. ??a and ??b. Excitation of the allowed EPR transition (fig. ??a) does not lead to simultaneous flips of
the electronic and nuclear spins, and is thus not capable of transferring polarization from the former to the latter. In contrast,
the ZQ and DQ forbidden transitions involve simultaneous electron-nucleus spin flips 1a and 1b. The current section aims to
illustrate the analytical strategy that we will employ to analyze the solid effect, in the simplest possible case of a single spin
1/2 (fig. ??b), and drive the solid-state DNP effect which is analyzed in this paper.

235 2.1 **Derivation of the rate equations**

While the forbidden transitions couple the nuclear and electronic polarizations, their influence on the latter is typically negligible
compared to other mechanisms of electronic relaxation. It is therefore justified to write a rate equation for 1a). We first present
the rate equation of the electronic polarization considering only the allowed EPR transition.

Below, we first examine the electronic transition on its own (fig and obtain its steady state (Sec. ??a) and then 2.1). Then we
240 turn to the electron-nucleus transitions (fig Bloch equations and also obtain their steady state (Sec. ??b). The derivation of the
rate equations is illustrated only for the mw excitation. Relaxation is included at the end by analogy 2.2). Finally, by requiring
that the two descriptions have identical steady states, we identify the rate constant that should be used to describe the effect of
the microwaves in the phenomenological rate equation.

2.0.1 **Allowed electronic transition**

245 2.1 Rate equation of the electronic polarization

Let n_+ and n_- be the populations of the two electronic spin energy levels in fig. ??1a. Assuming the spins are not destroyed
or created, the sum of the two populations is constant in time. Treating the mw excitation as a process that randomly flips the
spins with rate constant v_1 , we have

$$\dot{n}_+|_{\text{mw}} = -\dot{n}_-|_{\text{mw}} = -v_1(n_+ - n_-). \quad (1)$$

250 (The subscript of the vertical bar indicates that the time derivative accounts only for mw excitation.) Note that $v_1 \geq 0$, since a
negative rate constant does not make physical sense.

The electron-electronic spin polarization $P_S = (n_+ - n_-)/(n_+ + n_-)$ is negative at thermal equilibrium, i.e., $P_S^{\text{eq}} < 0$.
Differentiating P_S with respect to time and using (1), we find $\dot{P}_S|_{\text{mw}} = -2v_1 P_S$ -

for the effect of the mw irradiation. The action of thermal relaxation is analogous but, after replacing v_1 by w_{1S} and taking
255 into consideration that P_S decays towards its thermal equilibrium with rate $2w_{1S} = R_{1S} = 1/T_{1S}$, where T_{1S} is the electronic

T_1 -relaxation time. Combining: $\dot{P}_S|_{\text{th}} = -2w_{1S}(P_S - P_S^{\text{eq}})$. Combining the contributions of mw excitation and thermal relaxation we obtain the following rate equation for the electronic polarization:-

$$\dot{P}_S = -R_{1S}(P_S - P_S^{\text{eq}}) - 2v_1P_S.$$

, we get

$$260 \quad \dot{P}_S = -2v_1P_S - R_{1S}(P_S - P_S^{\text{eq}}), \quad (2)$$

where $R_{1S} = 2w_{1S}$. The electronic longitudinal relaxation time is $T_{1S} = 1/R_{1S}$.

Equation In the case of cw irradiation, one is interested in the steady state of the electronic polarization. When the left-hand side of (2) is depicted in is set equal to zero,

$$P_S^{\text{SS}} = \frac{R_{1S}}{R_{1S} + 2v_1} P_S^{\text{eq}} = p P_S^{\text{eq}}, \quad (3)$$

265 where the second equality defines the factor p . We refer to p as the electronic polarization factor, since it quantifies how close the steady-state polarization is to its Boltzmann value.

The rate equation (2) models the competition between mw pumping and the (longitudinal) relaxation of the polarization. When the two effects balance each other, the polarization is given by the steady-state solution (3). For the rate equation to be a predictive tool, it is necessary to express the phenomenological rate constants v_1 and w_{1S} in terms of more fundamental quantities. As discussed in the Introduction, these are identified with the probabilities of transition per unit time between the two energy levels in fig. ??e. In this graphical representation of 1a, which are calculated from time-dependent perturbation theory to first order (Solomon, 1955). In the case of v_1 , this is basically Fermi's golden rule (Shankar, 1994, Ch. 18), which contains the product of a squared matrix element and a shape-function that accounts for the fact that the energies of the two levels are not infinitely sharp (Abragam, 1961, Sec. IID). For a mw magnetic field in the x direction, the relevant matrix element is $w_{1S}(|S_x|^-)$. When the spread of the energy levels is identified with the EPR line shape, which we take to be a Lorentzian, one arrives at

$$270 \quad v_1(\Omega) = \frac{1}{2} \omega_1^2 \frac{R_{2S}}{R_{2S}^2 + \Omega^2}, \quad (4)$$

where $\Omega = \omega_S - \omega$ is the differential equation, we use an oval node to represent a dynamical variable (P_S in this case) whose time derivative is calculated by summing the contributions of all arrows that point into the node. The contribution of an arrow is obtained by multiplying the weight of the arrow by the variable from which the arrow originates. Differently from similar graphical representations in chemical kinetics, here an arrow does not deplete the node at its origin but only contributes to the node at its pointed end. By shading a node in gray we indicate that the corresponding variable remains constant in time. Each arrow in fig. ??e corresponds to one of the summands on the right-hand side of -. The two gray arrows account for thermal relaxation and the red arrow for mw excitation. offset of the mw frequency ω from the electronic resonance frequency ω_S , and R_{2S} is the electronic T_2 relaxation rate.

Energy levels of (a) single electronic spin ($S = 1/2$) and (b) one electronic spin and one nuclear spin ($I = 1/2$). Diagrammatic

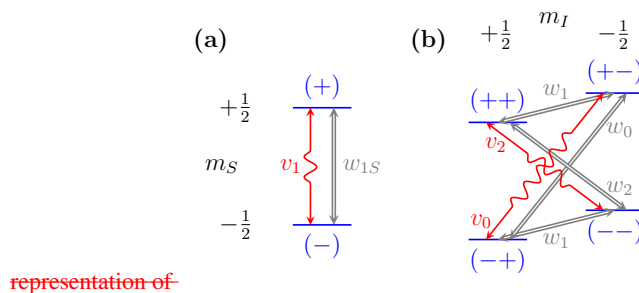


Figure 1. Energy levels of (a) a single electronic spin $S = 1/2$ and (b) one electronic spin and one nuclear spin $I = 1/2$. Microwaves excite single-, zero- and double-quantum transitions (wiggly red arrows) with rate constants v_1 , v_0 , and v_2 , respectively. Thermal relaxation (thick grey arrows) arises from coupling to external degrees of freedom.

We refer to arrows that leave a node and enter the same node as self-arrows. To prevent positive feedback, and thus ensure dynamical stability, the total contribution of all self-arrows of a node should not be positive. For the electronic polarization this means $R_{1S} + 2v_1 \geq 0$. (We always write the weight of a self-arrow with an explicit negative sign, which is placed inside the loop formed by the arrow.) Formally, this perturbative result is valid only for short times (Cohen-Tannoudji et al., 2019, Ch. XIII). Its validity at long times, including the steady state, thus needs to be explicitly established (Abragam, 1961, pp. 30-32). In the next subsection, we show that (4) is consistent with the steady state of the Bloch equations.

2.2 Bloch equations

The effect of the microwaves on the two-level system in fig. 1a is described exactly, and for all times, by the rate equations of (c) the electronic classical Bloch equations. The coherent part of these equations can be derived from the Liouville-von Neumann equation of the density matrix. Specifically, the evolution of the expectation value $q = \langle Q \rangle$ of a general spin operator Q , under the action of a spin Hamiltonian H (in units of angular frequency), is

$$\dot{q}|_{\text{coh}} = i\langle [H, Q] \rangle. \quad (5)$$

We describe the interaction of the electronic spins with the magnetic field using the following Hamiltonian in the rotating frame:

$$H = \Omega S_z + \omega_1 S_x. \quad (6)$$

Here the first term accounts for the Zeeman interaction with the constant magnetic field B_0 (along the z axis) and the second for the interaction with the mw field B_1 (along x).

Using (6) in (5), it is straightforward to obtain the coherent dynamics of $s_z = \langle S_z \rangle$, $s_y = \langle S_y \rangle$ and ~~(d) nuclear polarizations~~ $s_x = \langle S_x \rangle$. After appending transverse and longitudinal relaxation by hand, one arrives at the familiar Bloch equations

$$\begin{aligned} \dot{s}_x &= -\Omega s_y - R_{2S} s_x \\ \dot{s}_y &= \Omega s_x - \omega_1 s_z - R_{2S} s_y \\ 305 \quad \dot{s}_z &= \omega_1 s_y - R_{1S} (s_z - s_z^{\text{eq}}). \end{aligned} \quad (7)$$

Since the polarization P_S corresponds to the expectation value of the spin operator S_z , the rate equation (2) must be directly comparable to the third equation in (7). However, we see that the effect of the microwaves is modeled differently in the two equations. In the last Bloch equation, the microwaves couple s_z to the transverse component s_y . Such coupling is understandably missing in the rate equation, which describes the dynamics of P_S without reference to the transverse components. Clearly, the two descriptions cannot be equivalent in general. Nevertheless, in spite of the fundamentally different ways the two descriptions model the microwaves, there is a regime where the Bloch equations and the rate equation are equivalent, not only approximately but exactly. This is the regime of steady state.

At steady state, the transverse variables $s_{x,y}$ can be eliminated using the first two Bloch equations. From the first equation we find

$$315 \quad s_x^{\text{ss}} = -\frac{\Omega}{R_{2S}} s_y^{\text{ss}}, \quad (8)$$

where the superscript ‘ss’ denotes steady state. Substituting this result into the second Bloch equation, we get

$$s_y^{\text{ss}} = -\frac{\omega_1}{R_{2S} + \Omega \frac{1}{R_{2S}} \Omega} s_z^{\text{ss}}. \quad (9)$$

We have thus expressed both transverse components in terms of the longitudinal component as follows:

$$s_{x,y}^{\text{ss}} = \pm (\omega_1 f_{x,y}) s_z^{\text{ss}} \quad (10)$$

320 (the upper sign corresponds to x and the lower to y), where we have defined the auxiliary functions

$$f_y = \frac{1}{R_{2S} + \Omega \frac{1}{R_{2S}} \Omega}, \quad f_x = \frac{\Omega}{R_{2S}} f_y. \quad (11)$$

Finally, substituting s_y^{ss} into the third Bloch equation in (7), we arrive at the following differential equation for s_z at steady state:

$$s_z^{\text{ss}} = -\omega_1^2 f_y s_z^{\text{ss}} - R_{1S} (s_z^{\text{ss}} - s_z^{\text{eq}}). \quad (12)$$

325 Although the time derivative on the left-hand side of (12) equals zero, the equation was written in this form to facilitate its comparison with the rate equation (2). ~~(e) Rate equation of the electronic polarization at steady state and (f) its solution~~ Clearly,

if the rate constant v_1 in (2) is selected such that

$$2v_1 = \omega_1^2 f_y = \omega_1^2 \frac{1}{R_{2S} + \Omega \frac{1}{R_{2S}} \Omega}, \quad (13)$$

then the steady state of P_S will be identical to the steady state of s_z . Incidentally, the v_1 in (13), which ensures that the two descriptions have the same steady state, is identical to the rate constant obtained from first-order perturbation theory (eq. (4)). This will not be the case for the rate constants of the forbidden transitions, as we show in Sec. 3.

Once the two descriptions are demonstrated to have identical steady states, the analysis of the Bloch equations can be terminated at this point since it will exactly follow the steady-state analysis of the rate equation. In the next section, where we determine the ZQ and DQ transition rates from the steady state of the spin dynamics, we will similarly need to consider only the evolution of $i_z = \langle I_z \rangle$ under the action of the microwaves. The balance between the mw irradiation and the nuclear T_1 relaxation will be handled on the level of the rate equation of the nuclear polarization. ~~(g) Rate equation of the nuclear polarization at steady state. (a~~

For completeness, here we proceed one step further and solve (12) for s_z^{ss} recalling that the time derivative equals zero. The result is

$$s_z^{\text{ss}} = (R_{1S} f_z) s_z^{\text{eq}}, \quad (14)$$

where we have defined

$$f_z = \frac{1}{R_{1S} + \omega_1^2 f_y}. \quad (15)$$

The functions f_x , ~~b) Microwaves excite single-, zero- f_u and double-quantum transitions (wiggly red arrows) with rate constants v_1, v_0, f_z introduced in (11) and v_2 . Thermal relaxation (thick grey arrows) arises from coupling to external degrees of freedom, e.g., motion. (c-g) An arrow flowing into a node contributes either to (15) have units of time, and the factors enclosed in parenthesis in (10) and (14) are dimensionless. (This information is collected in Table 1.) Since (14) is equivalent to (3), it provides an expression for the polarization factor $p = 1 - s$, where s is the time derivative familiar saturation factor of the (allowed) electronic transition.~~

2.2.1 Forbidden transitions

Now we turn to the four-level system in

3 Forbidden transitions

The excitation of the allowed EPR transition considered above, does not lead to simultaneous flips of the electronic and nuclear spins, and is thus not capable of transferring polarization from the former to the latter. In contrast, the ZQ and DQ transitions involve simultaneous electron-nucleus spin flips (fig. ??b-1b), and drive the solid-state DNP effect. While these, so

Table 1. Functions characterizing the steady-state properties of the variable (oval node) or directly to classical Bloch equations and the variable (rectangular node). A gray node indicates that the variable is constant in time. (e,g) The sum Bloch-like equations of the arrows flowing into a gray oval node equals zero. variables $g_n = \langle S_n I_{\pm} \rangle$ ($f, g, n = x, y, z$) Dashed arrows are deduced relationships between the variables at steady-state.

| | <u>classical Bloch eqs.</u> | <u>Bloch-like eqs.</u> |
|----------------------|---|--|
| <u>unit of time</u> | <u>f_x, f_y, f_z</u> | <u>F_x, F_y, F_z</u> |
| <u>dimensionless</u> | <u>$\omega_1 f_x, \omega_1 f_y, R_1 S f_z$</u> | <u>$\omega_1 F_x, \omega_1 F_y, \delta F_z$</u> |

355 called, forbidden transitions couple the nuclear and electronic polarizations, their influence on the latter is typically negligible compared to other mechanisms of electronic relaxation. It is therefore justified to write a rate equation for the electronic polarization considering only the allowed EPR transition, as we did in Sec. 2. The effect of the mw-induced ZQ and DQ transitions on the nuclear polarization is described in the current section.

3.1 Rate equation of the nuclear polarization

360 Let n_{++} , n_{+-} , n_{-+} and n_{--} be the populations of the levels of the four-level system in fig. 1b. While their sum, $n = n_{++} + n_{+-} + n_{-+} + n_{--}$, remains constant in time, the individual populations change due to the ZQ and DQ transitions with rate constants v_0 and v_2 as follows:

$$\begin{aligned} \dot{n}_{-+}|_{\text{mw}} &= -\dot{n}_{+-}|_{\text{mw}} = -v_0(n_{-+} - n_{+-}) \\ \dot{n}_{++}|_{\text{mw}} &= -\dot{n}_{--}|_{\text{mw}} = -v_2(n_{++} - n_{--}). \end{aligned} \quad (16)$$

It is implicitly assumed that $v_0 \geq 0$ and $v_2 \geq 0$, as negative rate constants would not make physical sense.

365 The polarizations of the nuclear and electronic spins are

$$\begin{aligned} P_I &= [(n_{++} - n_{+-}) + (n_{-+} - n_{--})]/n \\ P_S &= [(n_{++} - n_{-+}) + (n_{+-} - n_{--})]/n. \end{aligned} \quad (17)$$

While, as before, $P_S^{\text{eq}} < 0$, the sign of P_I at thermal equilibrium will depend on the gyromagnetic ratio of the nuclear spin. We will assume protons, hence $\gamma_I > 0$ and $P_I^{\text{eq}} > 0$.

Differentiating Differentiating the definition of P_I in (17) with respect to time, and using (16), we obtain

370 $\dot{P}_I|_{\text{mw}} = -(v_2 + v_0)P_I - (v_2 - v_0)P_S,$

$$\begin{aligned} \dot{P}_I|_{\text{mw}} &= -v_0(P_I - P_S) - v_2(P_I + P_S) \\ &= -(v_2 + v_0)P_I - (v_2 - v_0)P_S \\ &= -v_+P_I - v_-P_S, \end{aligned} \quad (18)$$

which shows that mw excitation of the forbidden transitions couples the evolution of the nuclear polarization to the polarization of the electrons. This coupling is responsible for the ~~solid-state DNP effect.~~

375 ~~solid effect.~~ Because one always encounters either the difference or the sum of ~~the ZQ and DQ rate constants, we introduce~~
 ~~v_0 and v_2 , in the third equality of (18) we introduced~~

$$v_{\pm} = v_2 \pm v_0. \quad (19)$$

In fact, as we show later, the individual rates v_0 and v_2 may become negative, and thus meaningless from the rate-equation point of view.

380 ~~The two terms on the right-hand side of are represented by the two red arrows in fig. ??d. (The gray arrows correspond to thermal relaxation which is considered below.) For dynamical stability, $R_{1I} + v_{\pm} \geq 0$.~~

~~Of main interest for~~ ~~Although in~~ the current paper ~~are~~ ~~we are only interested in~~ the rates that describe the effect of the microwaves (i.e., the red arrows in fig. ??). ~~Nevertheless~~, we also discuss thermal relaxation as it is essential for reaching steady state.

385 Thermal relaxation of the nuclear spins due to their coupling to the electronic spins acts analogously to (18) after replacing the rates $v_{0,2}$ by $w_{0,2}$ and the polarizations by their deviations from thermal equilibrium. Further including nuclear T_1 relaxation due to mechanisms other than the coupling to the electrons, we arrive at

$$\begin{aligned} \dot{P}_I|_{\text{th}} = & -R_{1I}^0(P_I - P_I^{\text{eq}}) - 2w_1(P_I - P_I^{\text{eq}}) \\ & - w_+(P_I - P_I^{\text{eq}}) - w_-(P_S - P_S^{\text{eq}}), \end{aligned} \quad (20)$$

where R_{1I}^0 is the nuclear T_1 relaxation rate in the absence of the polarizing agent, ~~and~~

390 ~~$w_{\pm} = w_2 \pm w_0$~~

~~and~~, analogously to (19):

$$w_{\pm} = w_2 \pm w_0. \quad (21)$$

The cross-relaxation rate w_- is seen to couple the dynamics of P_I to P_S . This coupling ~~is responsible for the Overhauser DNP~~ ~~leads to the Overhauser~~ effect.

395 From (20), the total nuclear T_1 relaxation rate (i.e., in the presence of the free radical) is identified as $R_{1I} = R_{1I}^0 + 2w_1 + w_+$. Combining the contributions of mw excitation (eq. (18)) and relaxation (eq. (20)), we arrive at the following rate equation for the nuclear polarization:

$$\begin{aligned} \dot{P}_I = & -R_{1I}(P_I - P_I^{\text{eq}}) - w_-(P_S - P_S^{\text{eq}}) \\ & - v_+P_I - v_-P_S. \end{aligned} \quad (22)$$

~~This is the full differential equation depicted in fig. ??d.~~

400 3.2 Steady state of the rate equations

Although As the rate equations are only used in our analysis to describe the steady state, we solve (22) at steady state and describe the evolution of the electronic and nuclear polarizations in time, one is almost exclusively interested in their steady state (Webb, 1961). In fact, the only use of the rate equations appears to be in their steady state.

405 At steady state the time derivatives vanish and the dynamical variables settle at constant values, which we denote with the superscript 'ss'. In our diagrams, the node of a constant variable is shaded gray. Thus a gray oval node implies that the sum of all inflowing arrows equals zero. With this understanding, fig. ??e represents the rate equation of P_S at steady state.

Since the dynamics of the electronic polarization is decoupled from the polarization of the nuclei, the steady state of can be analyzed on its own. The condition that all inflowing arrows sum to zero yields

$$P_S^{ss} = \frac{R_{1S}}{R_{1S} + 2v_1} P_S^{eq} = p P_S^{eq},$$

410 where the second equality defines the factor p . (Observe how the weights of the two self-arrows in fig. ??e end up in the denominator.) This steady-state solution is depicted in fig. ??f.

We use a rectangular node when the inflowing arrows contribute directly to the value of the variable inside the node. (In contrast, when a variable is inside an oval node the arrows contribute to its time derivative.) The distinction between solid arrows and dashed arrows is that the former are reserved for fundamental, causal relationships between the variables which 415 dictate their dynamics at all times, while the dashed arrows indicate deduced mathematical relationships at steady state, which need not reflect direct causal links.

We will view the dashed arrow in fig. ??f as a transfer function that multiplies the variable at its input to produce the variable at its output. In this case the transfer function is $p = 1 - s$, where s is the familiar saturation factor of the (allowed) electronic transition. Since p quantifies how close the steady-state polarization is to its Boltzmann value (eq. express the nuclear 420 polarization under cw irradiation in terms of the equilibrium polarizations:

$$P_I^{ss} = \frac{R_{1I}}{R_{1I} + v_+} P_I^{eq} + \frac{sw_-}{R_{1I} + v_+} P_S^{eq} - \frac{pv_-}{R_{1I} + v_+} P_S^{eq}. \quad (23)$$

(We used (3)), we call it the electronic polarization factor, and use it interchangeably with $1 - s$ for the steady-state electronic polarization.)

425 Before turning to the steady state of the nuclear polarization, we observe that P_S and P_I reach steady state on time scales of the order of T_{1S} and T_{1I} , respectively. Since T_{1S} is typically much shorter than T_{1I} , there must be intermediate times where P_S has already reached steady state but P_I has not. Thus, it should be possible to replace P_S by P_S^{ss} in the rate equation of the nuclear polarization (eq.). Further using , we have

$$\dot{P}_I = -R_{1I}(P_I - P_I^{eq}) + sw_- P_S^{eq} - v_+ P_I - pv_- P_S^{eq}.$$

This rate equation at steady state is depicted in fig. ??g.

430 There are two links from P_S^{eq} to the derivative of P_I^{ss} . One of them scales with s and relies on the efficient saturation of the allowed EPR transition; the other scales with $p = 1 - s$. These two pathways correspond to the Overhauser and the solid-state DNP effects, respectively.

Solving the steady state of for the nuclear polarization, we get

$$P_I^{\text{ss}} = p_X \left[P_I^{\text{eq}} + \frac{sw_-}{R_{1I}} P_S^{\text{eq}} - \frac{pv_-}{R_{1I}} P_S^{\text{eq}} \right],$$

435 where we have defined the factor

$$p_X = \frac{R_{1I}}{R_{1I} + v_+}.$$

Because of its similarity to p in (3), we refer to p_X as the nuclear cross-polarization factor. Clearly, for large steady-state nuclear polarization, p_X should be as large as possible.

DNP is generally quantified through the enhancement of the nuclear polarization,

$$440 \quad \epsilon = P_I^{\text{ss}} / P_I^{\text{eq}} - 1, \quad (24)$$

which is defined such that it equals zero at thermal equilibrium. Taking into account that $P_S^{\text{eq}} / P_I^{\text{eq}} = -|\gamma_S| / \gamma_I$, where γ_S and γ_I are the gyromagnetic ratios of the electronic and nuclear spins, from (23) we obtain

$$\epsilon = \epsilon_X + \epsilon_{\text{OE}} + \epsilon_{\text{SE}},$$

where we have introduced the following

$$445 \quad \epsilon = \epsilon_{\text{SE}} + \epsilon_{\text{OE}} + (p_X - 1) \quad (25)$$

with

$$\epsilon_{\text{SE}} = \frac{pv_-}{R_{1I} + v_+} \frac{|\gamma_S|}{\gamma_I}, \quad \epsilon_{\text{OE}} = -\frac{sw_-}{R_{1I} + v_+} \frac{|\gamma_S|}{\gamma_I}$$

$$p_X = \frac{R_{1I}}{R_{1I} + v_+}. \quad (26)$$

The first two additive contributions to the DNP enhancement ϵ

$$\epsilon_{\text{SE}} = p_X \frac{pv_-}{R_{1I}} \frac{|\gamma_S|}{\gamma_I}, \quad \epsilon_{\text{OE}} = -p_X \frac{sw_-}{R_{1I}} \frac{|\gamma_S|}{\gamma_I}$$

$$\epsilon_X = p_X - 1.$$

450 ~~The first two correspond to~~ correspond to, respectively, the solid and Overhauser effects. The last one is due to neither of them. ~~When $p_X \neq 1$ (i.e., $v_+ \neq 0$) this term can shift the final enhancement by about one unit at most, and~~ Since it does not scale with the ratio of the gyromagnetic ratios, it should be negligible in most all cases of practical interest. Note that p_X is similar to the electronic polarization factor p in (3), but with R_{1S} and $2v_1$ replaced by R_{1I} and $v_0 + v_2$.

4 Spin dynamics

455 The above rate-equation analysis identified how different factors contribute to the DNP enhancement. However, for a quantitative understanding of the solid effect For the expressions in (26) to have a predictive value, it is necessary to know how the excitation rate constants v_{\uparrow} and express the rates v_{\pm} depend on the various experimental parameters. Such expressions are obtained in Sec. ?? after we analyze the relevant spin dynamics in the present section.

460 Quantum mechanically the polarizations P_S and P_I correspond to the expectations of the in terms of more fundamental quantities. This is done using first-order perturbation theory, under the assumption that the dipolar interaction between the electronic and nuclear spin operators S_z and I_z . The coherent evolution of the expectation value $q = \langle Q \rangle$ of a general spin operator Q , under the action of a spin Hamiltonian H (in units of angular frequency) is given by (Abragam, 1961)

$$\dot{q}|_{\text{coh}} = i\langle [H, Q] \rangle.$$

465 In this section we use to obtain equations of motion for the expectation values of the operators relevant to the solid effect. As in the previous section, we first analyze the electronic spins, and tackle the coupled electronic and nuclear spins after that.

3.1 Bloch equations

The interaction of the electronic spins with the magnetic field is described by the Hamiltonian

$$H = \Omega S_z + \omega_1 S_x,$$

470 where the first term accounts for the Zeeman interaction with the constant magnetic field B_0 , and spins is much smaller than the nuclear splitting (Abragam, 1955). Because the dipolar interaction mixes the Zeeman energy levels depicted in fig. 1b, the second term for the interaction with the mw field B_1 . The offset frequency $\Omega = \omega_S - \omega$ appears because the Hamiltonian is in the rotating frame.

475 Using with the Hamiltonian, one can determine the coherent dynamics of $s_z = \langle S_z \rangle$ ZQ and DQ transitions become weakly allowed. To first order, the mixed states are of the form $(--)+q(+-)$ (Abragam, 1955; Abragam and Proctor, 1958), with mixing parameter

$$q = \frac{1}{4} \frac{D_{\text{dip}}}{\omega_I} \frac{-3 \cos \theta \sin \theta e^{i\phi}}{r^3}. \quad (27)$$

Here, $D_{\text{dip}} = (\mu_0/4\pi)\hbar\gamma_S\gamma_I$ is the dipolar constant, $s_y = \langle S_y \rangle$ and $s_x = \langle S_x \rangle$. After appending electronic T_1 and T_2 relaxation by hand, one obtains the familiar Bloch equations

$$\dot{s}_x = -\Omega s_y - R_{2S} s_x$$

$$\dot{s}_y = \Omega s_x - \omega_1 s_z - R_{2S} s_y$$

$$\dot{s}_z = \omega_1 s_y - R_{1S} s_z + R_{1S} s_z^{\text{eq}}.$$

480 ~~These are depicted in fig. γ_S and γ_I are the gyromagnetic ratios of the spins, and (r, θ, ϕ) are the spherical polar coordinates of their relative position vector.~~

~~The probability amplitude of the microwaves to excite a transition between the mixed energy levels is then proportional to $\omega_1 q$. Combining the probability of excitation with the Lorentzian spread of the electronic energy levels, one arrives at the rate constants (Wind et al., 1985)~~

$$485 \quad v_{0,2}(\Omega) = 4(q^* q) v_1(\Omega \pm \omega_I), \quad (28)$$

~~where v_1 is the rate of the allowed (single-quantum) EPR transition (eq. 2a-(4)). In essence, the rates of the ZQ and DQ transitions are obtained by shifting the rate of the allowed transition along the frequency axis by $\pm\omega_I$, and reducing its magnitude through multiplication by $4|q|^2$.~~

490 ~~The two orange arrows in the figure correspond to the right-hand side of the first equation in and the three blue arrows to the second equation. The self-arrows of the oval nodes are due to T_1 and T_2 relaxation. The offset frequency leads to rotation in the x - y plane with angular velocity Ω . This corresponds to the loop formed by the orange and blue arrows with weights $-\Omega$ and $+\Omega$. Similarly, the loop formed by the blue and red arrows with weights $-\omega_I$ and $+\omega_I$ indicates rotation in the y - z plane with angular velocity ω_I due to the mw excitation.~~

~~Alternatively, one can form the dynamical variable $s_{\pm} = s_x + i s_y$ and work with the complex-valued Bloch equations~~

$$495 \quad \begin{aligned} \dot{s}_{+} &= -(R_{2S} - i\Omega)s_{+} - i\omega_1 s_z \\ \dot{s}_z &= -R_{1S}(s_z - s_z^{\text{eq}}) - \text{Re}\{i\omega_1 s_{+}\} \end{aligned}$$

~~which are depicted in fig. We observe that in this approach the rates of the forbidden transitions acquire a factor of ω_I^{-2} from $|q|^2$, and a factor of ω_1^2 from the mw excitation (eq. 2b. Notably, the rotation in the x - y plane with angular velocity Ω has now become the imaginary part of the self-arrow of s_{\pm} whose real part is (4), without any room for non-trivial cross-talk between these two frequencies. Such cross-talk is also not provided by the Lorentzian dependence on Ω . Like (28), the rate constants that we will obtain in the next subsection will also contain ω_1^2 and D_{dip}^2 as multiplicative factors. However, their offset dependence will couple ω_1 and ω_I in a non-trivial way, which reduces to the T_2 relaxation rate.~~

500 ~~In the complex-valued Bloch equations we have arbitrarily retained s_{\pm} and dropped s_{-} . Reducing the number of variables in this way simplifies the diagrammatic representation in fig. classical expression when $\omega_1 \ll \omega_I$ but predicts qualitatively different dependence when ω_1 is similar to or larger than ω_I (Sec. 2b compared to fig. 2a. (The simplification will be more substantial when we move to the analysis of the coupled electron-nucleus system.) Note however that the contribution of s_{-} is recovered when the real part of $i s_{\pm}$ is used to calculate the time derivative of s_z in the second line of (6.1).~~

505 ~~(a) Real-valued and (b) complex-valued classical Bloch equations and (c) corresponding dynamics according to the rate equation of the electronic polarization. (d) Spin dynamics of relevance to the solid effect and (e) corresponding dynamics implied by the rate equation of the nuclear polarization.~~

510 ~~In fig. 2c we recall the dynamics of s_z implied by the rate equation of the electronic polarization (fig. ??c). The visual comparison of this dynamics with the Bloch equations above it makes clear that the rate v_1 of the allowed EPR transition~~

is supposed to account in some effective way for the coupling between s_z and s_y (due to ω_I), and for the dynamics of the transverse components (due to Ω and R_{2S}). The rate constant v_I is thus expected to be a function of ω_I , Ω and R_{2S} .

3.1 Generalized Bloch equations for the solid effect

515 In this section, we obtain alternative expressions for the forbidden-transition rates v_{\pm} from the steady state of the exact quantum dynamics. We start by deriving equations of motion for the expectation values of the operators relevant to the solid effect. To use (5), we need to first specify the Hamiltonian guiding the dynamics.

3.2 Generalization to two coupled Bloch equations

~~To carry out a similar analysis for the nuclear polarization, we consider the~~ We will consider the minimal solid-effect spin
520 Hamiltonian (Wenckebach, 2016)

$$H = \Omega S_z + \omega_1 S_x - \omega_I I_z + \frac{1}{2}(A_1^* S_z I_+ + A_1 S_z I_-), \quad (29)$$

which is in the rotating frame for the electronic spin and in the laboratory frame for the nuclear spin. The first two terms are the same as in the Hamiltonian (6). The third term describes the nuclear Zeeman interaction. The sign of ω_I is negative since we assumed a nuclear spin with positive gyromagnetic ratio.

525 The last two terms in ~~the Hamiltonian~~ (29) account for the dipolar interaction between the electronic and nuclear spins. We have truncated this interaction by dropping all non-secular terms containing S_x and S_y . Similar to the assumption behind the derivation of the mixing factor (eq. (27)), we take the dipolar interaction to be small compared to the nuclear Zeeman splitting and drop the secular term proportional to $S_z I_z$. The remaining, pseudosecular terms scale with the dipolar coupling (Wenckebach, 2016)

$$530 \quad A_1 = D_{\text{dip}} \frac{-3 \cos \theta \sin \theta}{r^3} e^{i\phi} \quad (30)$$

where $D_{\text{dip}}/2\pi \approx 79.066 \text{ kHz nm}^3$ for protons. The subscript of A_1 indicates that its angular dependence is identical to the second-degree spherical harmonic of order $m = 1$.

We start our derivation of equations of motion with $i_z = \langle I_z \rangle$, as it corresponds to the nuclear polarization. There is no contribution from the first three terms in the Hamiltonian (29) as I_z commutes with all of them (eq. (5)). From the commutator
535 with the dipolar terms we obtain

$$\dot{i}_z|_{\text{coh}} = i \frac{1}{2} (A_1 g_z^* - A_1^* g_z) = -\text{Re}\{i A_1^* g_z\}, \quad (31)$$

where

$$g_n = \langle S_n I_+ \rangle \quad (n = x, y, z). \quad (32)$$

Proceeding in the same way, we first find

$$540 \quad \dot{g}_z|_{\text{coh}} = -i\omega_I g_z + \omega_1 g_y - i(A_1/4)i_z \quad (33)$$

and then

$$\begin{aligned}\dot{g}_y|_{\text{coh}} &= \Omega g_x - i\omega_I g_y - \omega_1 g_z + (A_1/4)s_x \\ \dot{g}_x|_{\text{coh}} &= -i\omega_I g_x - \Omega g_y - (A_1/4)s_y.\end{aligned}\tag{34}$$

The chain of dynamical equations can be terminated at this stage, as $s_{x,y}$ obey the classical Bloch equations discussed above. (The dynamics of the electronic spin was taken to be independent of its dipolar coupling with the nuclei.)

545 In addition to the coherent evolution considered so far, $g_z = \langle S_z I_+ \rangle$ and $g_{x,y} = \langle S_{x,y} I_+ \rangle$ are expected to decay with rates $R_{1S} + R_{2I}$ and $R_{2S} + R_{2I}$, respectively. Neglecting R_{2I} compared to R_{1S} and R_{2S} , we arrive at the following system of coupled differential equations:

$$\begin{bmatrix} \dot{g}_x \\ \dot{g}_y \\ \dot{g}_z \end{bmatrix} = -\mathcal{B} \begin{bmatrix} g_x \\ g_y \\ g_z \end{bmatrix} - i\frac{1}{4}A_1 \begin{bmatrix} -is_y \\ is_x \\ iz \end{bmatrix},$$

with-

$$550 \quad \mathcal{B} = \begin{bmatrix} R_{2S} + i\omega_I & \Omega & 0 \\ -\Omega & R_{2S} + i\omega_I & \omega_1 \\ 0 & -\omega_1 & R_{1S} + i\omega_I \end{bmatrix}.$$

~~This matrix is essentially the familiar Bloch matrix of the real-valued Bloch equations but with $i\omega_I$ added to its main diagonal.~~

$$\begin{aligned}\dot{g}_x &= -(R_{2S} + i\omega_I)g_x - \Omega g_y - (A_1/4)s_y \\ \dot{g}_y &= \Omega g_x - (R_{2S} + i\omega_I)g_y - \omega_1 g_z + (A_1/4)s_x \\ \dot{g}_z &= -(R_{1S} + i\omega_I)g_z + \omega_1 g_y - i(A_1/4)iz.\end{aligned}\tag{35}$$

Equations (31) and (35), supplemented by the Bloch equations (7), constitute the generalization of the Bloch equations to the four-level system in fig. 1b as relevant to the solid effect. If desired, one can also supplement (31) with nuclear T_1 relaxation. However, because our aim is to identify the ~~forbidden-transition~~ rates v_{\pm} , this is not necessary. In any case, ~~we already analyzed~~ the balance between thermal relaxation and mw excitation at steady state was already analyzed using the rate-equation formalism (Sec. 63.1).

~~Equations~~ Analogously to our treatment of the Bloch equations (Sec. 2.2), we will now use the condition of steady state to eliminate all variables except the polarizations i_z and s_z . From the steady state of the first equation in (35) we get

$$560 \quad g_x^{\text{ss}} = -\frac{\Omega}{R_{2S} + i\omega_I} g_y^{\text{ss}} - \frac{A_1/4}{R_{2S} + i\omega_I} s_y^{\text{ss}}.\tag{36}$$

Substituting into the second equation of (35) we find

$$g_y^{\text{ss}} = -\omega_1 F_y g_z^{\text{ss}} + (A_1/4)(F_y s_x^{\text{ss}} - F_x s_y^{\text{ss}}),\tag{37}$$

where we introduced the complex-valued functions

$$F_y = \frac{1}{R_{2S} + i\omega_I + \Omega \frac{1}{R_{2S} + i\omega_I} \Omega}$$

$$F_x = \frac{\Omega}{R_{2S} + i\omega_I} F_y, \quad (38)$$

565 which generalize the functions (11) of the classical Bloch equations by supplementing their relaxation rates with an imaginary part. Like their real analogs, $F_{x,y}$ have units of time (Table 1).

Substituting g_y^{ss} into the last equation of (35) and solving for g_z at steady, we find

$$g_z^{\text{ss}} = -i(A_1/4)F_z i_z^{\text{ss}} + (A_1/4)F_z(\omega_1 F_y s_x^{\text{ss}} - \omega_1 F_x s_y^{\text{ss}}), \quad (39)$$

where the function

$$570 F_z = \frac{1}{R_{1S} + i\omega_I + \omega_1^2 F_y} \quad (40)$$

generalizes (15) of the classical Bloch equations. Finally, we substitute g_z^{ss} into the equation of i_z (eq. (31)). Factoring out the dipolar coupling as

$$\delta^2 = (A_1^* A_1)/4, \quad (41)$$

at steady state (31) becomes

$$575 i_z^{\text{ss}}|_{\text{coh}} = -\delta^2 \text{Re}\{F_z\} i_z^{\text{ss}} - \delta^2 \text{Re}\{iF_z(\omega_1 F_y)\} s_x^{\text{ss}} - \delta^2 \text{Re}\{iF_z(-\omega_1 F_x)\} s_y^{\text{ss}}. \quad (42)$$

We have thus managed to eliminate the three electron-nucleus coherences g_{ν} .

To further eliminate the electronic coherences from (42), we recall that at steady state the transverse components $s_{x,y}$ are algebraically related to s_z (eq. (10)). Hence,

$$i_z^{\text{ss}}|_{\text{coh}} = -\delta^2 \text{Re}\{F_z\} i_z^{\text{ss}} - \delta^2 \omega_1^2 \text{Re}\{iF_z(F_y f_x + F_x f_y)\} s_z^{\text{ss}}. \quad (43)$$

580 As the right-hand side of (43) contains only i_z and s_z , supplemented by the Bloch equations, constitute the generalization of the Bloch equations to the four-level system in fig. 6, it can be directly compared with the rate equation (18), which accounts for the contribution of the microwaves to the time derivative of P_I . The comparison allows us to identify the two phenomenological rate constants of the forbidden transitions as

$$v_+ = \delta^2 \text{Re}\{F_z\}, \quad v_- = \delta^2 \omega_1^2 \text{Re}\{iF_z(F_y f_x + F_x f_y)\}. \quad (44)$$

585 When used with these two rate constants, the rate equation of P_I is guaranteed to have the correct steady state.

The above non-perturbative derivation of the rate constants v_{\pm} is the main analytical contribution of the current paper. In Sec. ??b as relevant to the solid effect. This system of equations is depicted in 6, we will explore the predictions of these expressions, as well as their relationship with the classical perturbative rates (eq. (28)). Before that, in the next section, we revisit the equations of motion (31), (35), and the Bloch equations (7), which constitute a system of seven coupled differential

590 equations. The steady state of this system of equations is examined in Sec. 5.

4 Making sense of the spin dynamics

The Bloch equations (eq. (7)) are coupled differential equations describing the time evolution of three dynamical variables. When the number of coupled equations is small, it is possible to form a mental picture of the dynamical interconnections between the variables by examining the written equations. In the case of more than three variables, however, gaining insight into the dynamics by simply looking at the written equations becomes harder.

The need to make sense of several coupled differential equations also arises in the context of chemical reaction kinetics, where the concentrations of the reactants change in time. When the number of chemical species is small, it is sufficient to write down the kinetic equations for the concentrations. However, when one deals with the reactions of even a relatively simple metabolic pathway, like glycolysis or the citric acid cycle, the rate equations are almost never written down explicitly. Instead, they are represented in a visual way by drawing arrows between the names of the chemical species that are interconverted by the reactions.

Following the same logic, we represent the dynamical variables s_x , s_y and s_z of the classical Bloch equations (7) as nodes, and the various interactions that couple their dynamics as arrows (fig. 2d, where blue, orange and green arrows a). The time derivative of each variable is calculated by summing the contributions of all arrows that point into its node, where the contribution of an arrow is obtained by multiplying the weight of the arrow by the variable from which it originates. Differently from the representation of chemical reactions, here an arrow does not deplete the node at its origin but only contributes to the node at its pointed end. In addition, as our arrows do not have the physical interpretation of reaction rate constants, their weights may also be negative.

The two orange arrows in fig. 2a, which flow into the nodes g_x , g_y and g_z , respectively. Black arrows node of s_x , correspond to the two terms on the right-hand side of the first Bloch equation in (7). The arrow with weight $-\Omega$ originates from s_y , and thus contributes $-\Omega s_y$ to the time derivative of s_x . The other orange arrow originates from s_x and accounts for the decay of this variable with the rate constant R_{2S} of the transverse relaxation. We refer to such arrows that leave a node and enter the same node as self-arrows. To prevent positive feedback, and thus ensure dynamical stability, the total contribution of self-arrows (in case several such arrows point into a node) should be positive. We will generally write the weight of a self-arrow with an explicit negative sign, which we place inside the loop formed by the arrow.

Similarly, the three blue arrows in fig. 2a, which flow into the node of s_y , correspond to the classical Bloch equations: three terms on the right-hand side of the second Bloch equation in (7). The remaining three arrows, which flow into s_z , correspond to the right-hand side of the last Bloch equation. Rather than using the same color for these three arrows, we have indicated the contribution of mw irradiation with red and the contribution of relaxation with gray, in line with the colors used in fig. 1a. In any case, the colors of the arrows do not play a role in the correspondence between the differential equation and its visual representation. Because the equilibrium value s_z^{eq} is a constant parameter in the Bloch equations, there are no arrows flowing into its node. A node is shaded gray when the corresponding variable remains constant in time.

For comparison, in While fig. 2a contains exactly the same information as the Bloch equations (7), all dynamical interconnections between the variables are now visually accessible. For example, the loop formed by the two arrows with weights $-\omega_1$ and ω_1

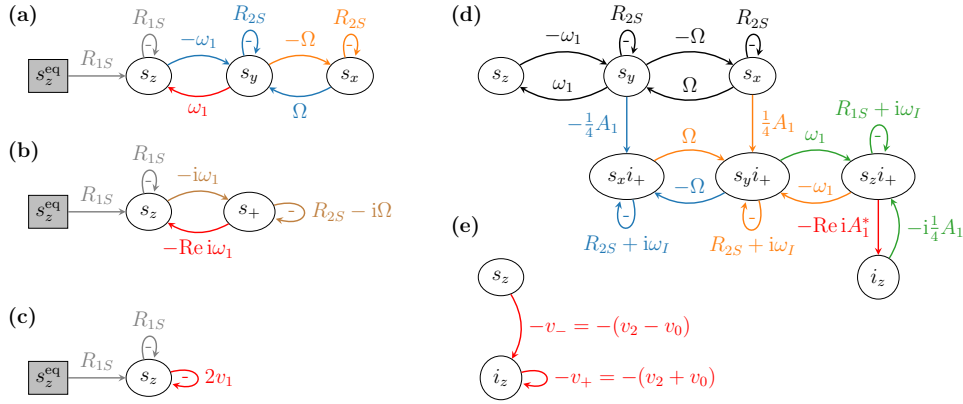


Figure 2. (a) Real-valued and (b) complex-valued classical Bloch equations and (c) corresponding dynamics according to the rate equation of the electronic polarization. (d) Spin dynamics of relevance to the solid effect and (e) corresponding dynamics implied by the rate equation of the nuclear polarization.

625 between the variables s_y and s_z , corresponds to rotation in the y - z plane with angular velocity equal to ω_1 . In other words, this loop is a visual manifestation of the Rabi nutation driven by the microwaves. There is a similar loop between the variables s_x and s_y , which corresponds to rotation with angular velocity Ω in the x - y plane. This is the Larmor precession, as seen in the rotating frame. Since all other arrows correspond to relaxation, the diagram in fig. 2e we recall the description of the same spin dynamics according to the rate-equation formalism (red arrows in a confirms in a visual way that the coherent part of the Bloch equations consists of two rotations.

At this point we mention that instead of working with the real-valued Bloch equations (7), one could form the dynamical variable $s_+ = s_x + is_y$ and work with the complex-valued Bloch equations

$$\begin{aligned} \dot{s}_+ &= -(R_{2S} - i\Omega)s_+ - i\omega_1 s_z \\ \dot{s}_z &= -R_{1S}(s_z - s_z^{\text{eq}}) - \text{Re}\{i\omega_1 s_+\}. \end{aligned} \quad (45)$$

635 These two differential equations are depicted in fig. 2b. Notably, the rotation in the x - y plane with angular velocity Ω (i.e., the Larmor precession) has now become the imaginary part of the self-arrow of s_+ whose real part is the T_2 relaxation rate.

In (45) we arbitrarily retained s_+ and dropped s_- , thus reducing the number of variables in the diagrammatic representation from three to two. (The analogous reduction will be more substantial in the case of the coupled electron-nucleus system.) Note, however, that the contribution of s_- is recovered when the real part of is_+ is evaluated to calculate the time derivative of s_z in the second line of (45).

640 In fig. ??d). Evidently, the two rates v_{\pm} are expected to summarize in some faithful way the complexity of the proper, quantum-mechanical dynamics in 2c we have represented the dynamics of s_z which is implied by the rate equation of the electronic polarization (eq. (2)). The visual comparison of this dynamics with the Bloch equations above it makes clear that the rate v_1 of the allowed EPR transition is supposed to account in some effective way for the coupling between s_z and s_y (due to

645 ω_1), and for the dynamics of the transverse components (due to Ω and R_{2S}). Indeed, the rate constant v_1 in (13) is a function of ω_1 , Ω and R_{2S} .

In fig. 2d we show the system of seven coupled differential equations that play a role in the solid effect (eqs. (31), (35) and the Bloch equations). For clarity, the nodes of g_n ($n = x, y, z$) are labeled as $s_n i_+$ in the figure. Black arrows correspond to the classical Bloch equations. Blue, orange and green arrows, which flow into the nodes g_x , g_y and g_z , respectively, correspond to the right-hand sides of the three equations in (35). The red arrow flowing into the node of i_z corresponds to the right-hand side of (31). Note that the weight of the red arrow involves taking a real part, just like in the complex-valued Bloch equations. Thus, although we only show the dynamics of the coherences $S_n I_+$, at this point the effect of the coherences $S_n I_-$ is also included. In other words, if we did not take the real part, we would need to represent ten coupled differential equations, rather than seven.

The graphical representation of the spin dynamics in fig. 2d provides visual access to many aspects of the solid effect. Regarding the overall organization, we notice that the classical lays bare the overall topology of the dynamical connections between the seven variables. For example, note that the Bloch-equations pattern connecting the top three nodes (black arrows) is recapitulated between the nodes of the coherences g_n ($n = x, y, z$) below them. As a result, there are two sets of Bloch equations which are connected back to back, with the y variable of one of them feeding into the x variable of the other, and vice versa. The connection between these two set is established by the dipolar coupling (A_1). Indeed, between the electron-nucleus coherences one recognizes the loops that correspond to Rabi nutation and Larmor precession. Due to the involvement of the nuclear spin operator I_+ , the this second set of Bloch equations is “shifted” by the nuclear Larmor frequency, as evidenced by the imaginary part of the self-arrows of g_n . The link between the electronic Bloch equations and these new Bloch equations that describe the dynamics of the S - I coherences is established by the dipolar coupling (A_1), which connects the two sets of Bloch equations such that the y variable of one of them feeds into the x variable of the other, and vice versa. The same dipolar interaction also connects g_z to the nuclear polarization through the red arrow in fig. 2d. Although the coherences $S_n I_-$ are not explicitly modeled, their contribution is recovered when we feed the real value of $i A_1^* g_z$ a real value into the time derivative of i_z , as discussed above. At this stage, Bloch-like equations shifted by $+\omega_I$ and (shown) and by $-\omega_I$ contribute symmetrically (not shown) contribute symmetrically to the nuclear polarization.

Turning attention to the pathways bridging All interactions in the Hamiltonian (29) lead to rotations, which are manifested as loops between two variables formed by arrows with opposite weights. Although such loops are also formed between the variables s_y and g_x , and between s_x and g_y , we have not shown the arrows that originate at g_x and g_y and flow into, respectively, s_y and s_x . These arrows, which would complete the loops of the dipolar interaction, are dropped because their contribution to the electronic dynamics is neglected.

For comparison, in fig. 2e we recall the description of the same spin dynamics according to the rate-equation formalism (eq. (18)). Clearly, the two rates v_{\pm} should summarize in some faithful way the complexity of the proper, quantum-mechanical dynamics in fig. 2d. In particular, the rate v_- should account for the pathways from s_z to i_z , and the rate v_+ for the pathways from i_z into the coherences g_n and back to i_z .

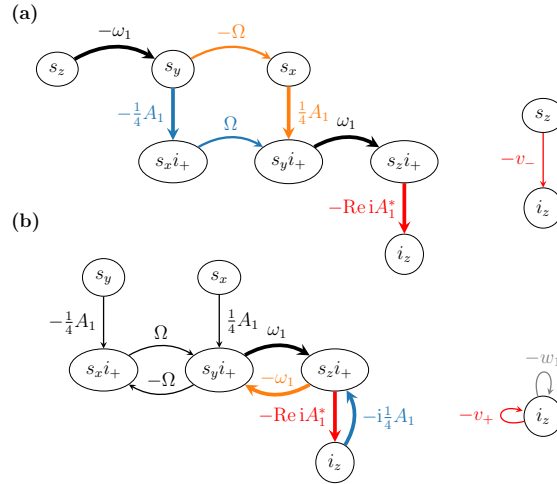


Figure 3. Pathways (a) from s_z to i_z contributing to the rate v_- and (b) from i_z to i_z contributing to the rate v_+ .

By examining the pathways from s_z to i_z we gain visual understanding of the mechanism of the dynamical coupling between the electronic and nuclear polarizations in the solid effect. Following The two possible paths for reaching i_z from s_z following the “flow” of the arrows are shown in fig. 3a. Both paths consists of four steps, i_z is reached from s_z in four steps (not counting the mixing of the transverse components by $\pm\Omega$). First, the mw excitation (ω_1) generates the transverse components $s_{x,y}$ from s_z . This step is described by the classical Bloch equations. Then, from $s_{x,y}$ the dipolar coupling (A_1) generates the coherences $s_{x,y}i_+$ from $s_{y,x}$. These are then converted to $s_z i_+$ by the mw excitation, and finally the dipolar interaction transforms $s_z i_+$ to i_z . Because Observe that the weights ω_1 and A_1 appear twice along the path from s_z to i_z , the net efficiency of the solid effect scales with the squares of both ω_1 and A_1 each path, thus both paths scale as $\omega_1^2 |A_1|^2$. Since these paths contribute to the rate constant v_- , it should also scale with the mw power and the square of the dipolar interaction, which is in agreement with the perturbative rates in (28).

Additionally, we observe that all paths from s_z to i_z traverse the In addition to the weights considered above, both paths in fig. 3a also traverse arrows with weights $\pm\Omega$. Thus, on resonance (i.e., $\Omega = 0$), the possibility of polarization transfer is severed. This observation does not appear to be particularly useful as driving the forbidden transitions requires are driven at $\Omega \approx \pm\omega_I$ anyway. However, as since going along an arrow with weight $\pm\Omega$ amounts to multiplication by Ω , we realize that crossing from the left side of the dynamical network to the right side involves change of parity in Ω . In other words, because s_z is an even function of the frequency offset, its effect on i_z must be odd in Ω . This is the reason for the anti-symmetric field profile of the solid effect (in contrast to the symmetric profile of the Overhauser effect). The diagram makes clear that the solid effect is odd in Ω for the same reason that s_x is odd, as intuited by Erb, Motehane and Uebersfeld (Erb et al., 1958a). This point is further examined in Sec. 5.

The above observations were related to the paths from s_z to i_z , which contribute to the rate v_- (

In fig. 2e). Examining the paths 3b we have highlighted the arrows that contribute to the self-loop of i_z with weight v_+ ; we see that. Again there are two possibilities: one consisting of two steps and the other of four (fig. 2d). The shorter path from i_z to g_z (blue arrow), and back to i_z (red arrow), relies only on the dipolar coupling interaction between the electronic and nuclear spins, and must be active even in the absence of mw excitation. The longer path additionally goes from g_z to $g_{x,y}$ (the latter are mixed by Ω) and back, and contributes only under mw irradiation. Considering the separate treatment of that thermal relaxation and mw excitation are treated separately, we realize that the short loop in fact contributes to the nuclear T_1 relaxation (more precisely to the rate w_1 in fig. ??1b), hence its contribution should be removed when calculating the rate v_+ .

These general observations are developed in more detail below.

5 Excitation rate constants

It is clear that the polarization dynamics in fig. On the basis of this observation, we now modify the analytical expression for v_+ that we gave in (44). Since the nuclear T_1 is typically measured with the microwaves switched off, we identify the ω_1 -independent part of F_z (eq. 2c could approximate the Bloch equations in fig. 2a only under some special conditions. For example, if the T_{2S} and T_{1S} relaxation times are well separated, it is possible to eliminate the fast variables $s_{x,y}$ from the Bloch equations and thus obtain a closed dynamical equation for the slow variable s_z , which will be valid at times longer than the fast time scale T_{2S} (Van Kampen, 1985). Similarly, the reduced dynamics in fig. 2e could be a good approximation of the true dynamics in fig. 2d under some conditions. (40)), namely

$$F_z(\omega_1 = 0) = (R_{1S} + i\omega_I)^{-1}, \quad (46)$$

as contributing to relaxation. The corrected form of the first equality in (44) is thus

$$v_+ = \delta^2 \text{Re}\{F_z - (R_{1S} + i\omega_I)^{-1}\}. \quad (47)$$

Having a visual representation of the spin dynamics was thus helpful to identify an aspect that would be harder to identify on the level of the written equations.

If, however, the reduced equations are not required to provide a faithful description of the dynamics, there is a regime in which they are exact without any additional requirements. This is the regime of steady state. In fact, since the use of the rate equations from Sec. ?? lies in the steady state that they describe, and not in the dynamics that they unwittingly imply, nothing is sacrificed by confining them to steady state.

In this section we analyze the steady state of the quantum-mechanical equations of motion (Sec. 4) and compare it with the steady state of the rate equations (Sec

5 Analyzing the steady state

730 The diagrammatic representations of the previous section showed that the quantum-mechanical dynamics consists of several simultaneous rotations that mix the expectation values of the various spin operators. In spite of the complicated time evolution that such interconnected rotations may generally lead to, relatively simple algebraic relationships between the variables emerged at steady state (Secs. 6). The comparison will allow us to identify the phenomenological rate constants v_1, v_{\pm} in terms of the parameters of the spin dynamics.

5.1 Steady state of the Bloch equations

At steady state, the sum of all arrows flowing into an oval node equals zero. Shading the oval nodes (2.2 and 3.1).

735 The steady-state relationships of the Bloch equations, which were given in (10) and (14), are depicted diagrammatically in fig. 2ain gray, we arrive at fig. ??a which represents the classical Bloch equations at steady state. The condition that the two orange arrows flowing into s_x^{ss} sum to zero yields

$$s_x^{ss} = -\frac{\Omega}{R_{2S}} s_y^{ss}.$$

(Observe how the weight of the self arrow of s_x^{ss} ends up in the denominator.) This steady-state relationship is depicted by 4a. Because we deal with algebraic (as opposed to differential) equations, the inflowing arrows now contribute directly to the black dashed arrow in fig. ??b. value of the variable inside the node, and not to its time derivative. To make this distinction visually clear, we use a rectangular node when the variable itself is obtained by adding the contributions of all inflowing arrows. In addition, we use dashed arrows to signal that the mathematical relationships hold only at steady state. In contrast, the solid arrows of the previous section represented fundamental, causal relationships between the variables governing their dynamics at all times.

745 Using one can eliminate s_x^{ss} from the differential equation of s_y (second equation in). The remaining two equations, which contain only the variables s_y^{ss} and s_z^{ss} , are represented in fig. ??b. The elimination of s_x^{ss} resulted in the self-arrow of s_y^{ss} drawn with a dashed blue line.

Proceeding further, we now express s_y^{ss} in terms of s_z^{ss} using the second Bloch equation in:

$$s_y^{ss} = -\frac{\omega_1}{R_{2S} + \Omega \frac{1}{R_{2S}} \Omega} s_z^{ss}.$$

750 (Again the self-arrows of the eliminated node end up in the denominator.) This relation is represented by the black dashed arrow in

It is convenient to think of the steady-state Bloch equations as a system that takes the Boltzmann polarization s_z^{eq} as an input and produces the outputs $s_{x,y}^{ss}$ as suggested graphically in fig. ??e. Using we now eliminate s_y^{ss} from the equation of s_z^{ss} (last equation in). The term that contained s_y^{ss} corresponds to the self-arrow of s_z^{ss} which is shown with red dashed arrow in fig. ??e.

Visual comparison of the remaining equation of s_z^{ss} (4a. Each dashed arrow can thus be viewed as a transfer function that multiplies the variable at its input to produce the variable at its output. The weights of the arrows in fig. ??e) with fig. 2e

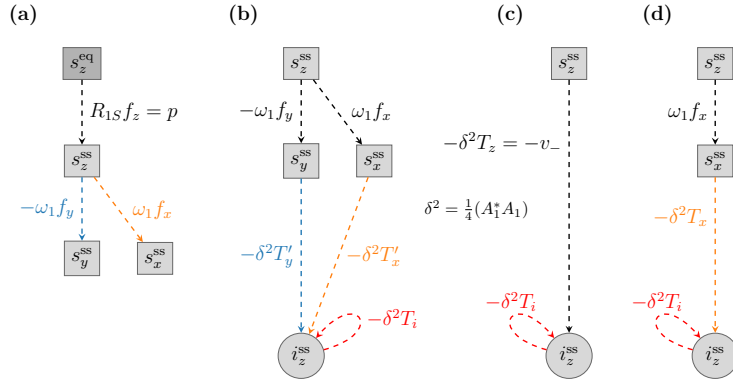


Figure 4. Algebraic relations between the dynamical variables at steady state. (a) Real-valued-Transfer functions of the Bloch equations at steady state. (b) Elimination of s_x^{ss} . (c) Further elimination of s_y^{ss} . (d) Solution for s_z^{ss} . Transfer functions describing the steady-state relationship between the time derivative of i_z (eoutput) Steady-state solution and different choices of the Bloch equations with the dashed arrows viewed as transfer functions electronic input.

directly yields-

$$v_1 = \frac{1}{2} \omega_1^2 \frac{R_{2S}}{R_{2S}^2 + \Omega^2}$$

760 for the rate constant of the allowed EPR transition. This result agrees with . Our derivation makes clear that this functional dependence of v_1 on ω_1 , R_{2S} and Ω is, in fact, exact at steady state. 4a are dimensionless (Table 1).

If the purpose is to determine the rate constant v_1 , the analysis can be terminated at this point without ever encountering the T_1 relaxation of the electronic spins. Below, when we determine Equation (43), from which we identified the rates v_{\pm} , we will similarly need to consider only the coherent evolution of i_z without worrying about the nuclear T_1 relaxation. In fact, once the
 765 rate constants of mw excitation are identified, the steady-state analysis is identical to the one we already carried out in See is depicted in fig. ?? for the rate equations of the polarizations.

For completeness, here we proceed one step further and solve the equation for s_z^{ss} by moving the self-arrows 4b and, equivalently, in fig. ?? to the denominator:

$$s_z^{ss} = \frac{R_{1S}}{R_{1S} + \omega_1 \frac{1}{R_{2S} + \Omega} \frac{1}{R_{2S}} \Omega} s_z^{eq}.$$

770 This result (fig. ??d) is equivalent to 4c.

The above successive elimination of the variables from the steady-state Bloch equations (figs The three colored arrows in fig. ??b-d) is just the poor man's inversion of the Bloch matrix. Nevertheless, it allowed us to follow the step-by-step emergence

of the functions-

$$f_y(\Omega) = \frac{1}{R_{2S} + \Omega \frac{1}{R_{2S}} \Omega}, \quad f_x(\Omega) = \frac{\Omega}{R_{2S}} f_y(\Omega)$$

$$h(\omega_1, \Omega) = \frac{1}{R_{1S} + \omega_1 f_y(\Omega) \omega_1},$$

775 which have units of time (Table 1, first row). In terms of these functions, the ratios between the variables of the Bloch equations at steady state are

$$\frac{s_{x,y}^{ss}}{s_z^{ss}} = \pm \omega_1 f_{x,y}(\Omega), \quad \frac{s_z^{ss}}{s_z^{eq}} = R_{1S} h(\omega_1, \Omega) = p.$$

(The last equality follows from .) These ratios are depicted as transfer functions in 4b correspond to the three terms on the right-hand side of (42), before the transverse components $s_{x,y}^{ss}$ were replaced by s_z^{ss} . Specifically,

$$780 \quad T_i = \text{Re}\{F_z\}, \quad T'_x = \text{Re}\{iF_z(\omega_1 F_y)\}, \quad T'_y = \text{Re}\{iF_z(-\omega_1 F_x)\}. \quad (48)$$

The cumulative transfer function from s_z to i_z (fig. ??e. Note that the weights of the dashed arrows are dimensionless, as they equal the product of a variable with units of inverse time and a function with units of time (Table 1, second row). For our purposes it will be convenient to think of the steady-state Bloch equations as a system that takes s_z^{eq} as an input and produces the outputs $s_{x,y}^{ss}$, as suggested graphically 4c) is obtained by adding the contributions of the two parallel paths in fig. ??e-4b.

785 The sum

$$T_z = \omega_1 f_x T'_x - \omega_1 f_y T'_y$$

$$= \omega_1^2 \text{Re}\{iF_z(F_y f_x + F_x f_y)\} = v_- / \delta^2 \quad (49)$$

was already evaluated in (43).

Functions characterizing the steady-state properties of the two sets of Bloch equations: classical Bloch eqs. second Bloch eqs. unit of time f_x, f_y, h, F_x, F_y, H dimensionless $\omega_1 f_x, \omega_1 f_y, R_{1S} h, \omega_1 F_x, \omega_1 F_y, \delta H$

790 5.1 Bloch equations

To examine the properties of this system steady-state properties of the Bloch equations, in fig. 5 we plot its transfer functions the ratios $s_z^{ss}/s_z^{eq} = p(\Omega, \omega_1)$ (first row) and $s_{x,y}^{ss}/s_z^{ss} = \pm \omega_1 f_{x,y}(\Omega)$ (second row) against the offset frequency Ω for four different values of B_1 . A free radical with $g = 2$ was assumed when converting B_1 to ω_1 , so that $B_1 = 6$ G corresponds to $\omega_1/2\pi = 16.8$ MHz. This maximum value of B_1 is intended to reflect the actual mw field of modern-day DNP spectrometers at X band (Neudert et al., 2016) and at J band (Kuzhelev et al., 2022). The electronic relaxation times used in the plots were $T_{2S} = 60$ ns and $T_{1S} = 9T_{2S} T_{1S} = 9T_{2S} = 540$ ns.

The From the first row of fig. 5 shows the transfer function $R_{1S} h$, which is the electronic polarization factor under mw power. The we see that the electronic saturation is most efficient on resonance ($\Omega = 0$) and quickly becomes inefficient at larger offsets. With increasing mw power (different columns) the deviation of s_z^{ss} from equilibrium spreads to larger offsets.

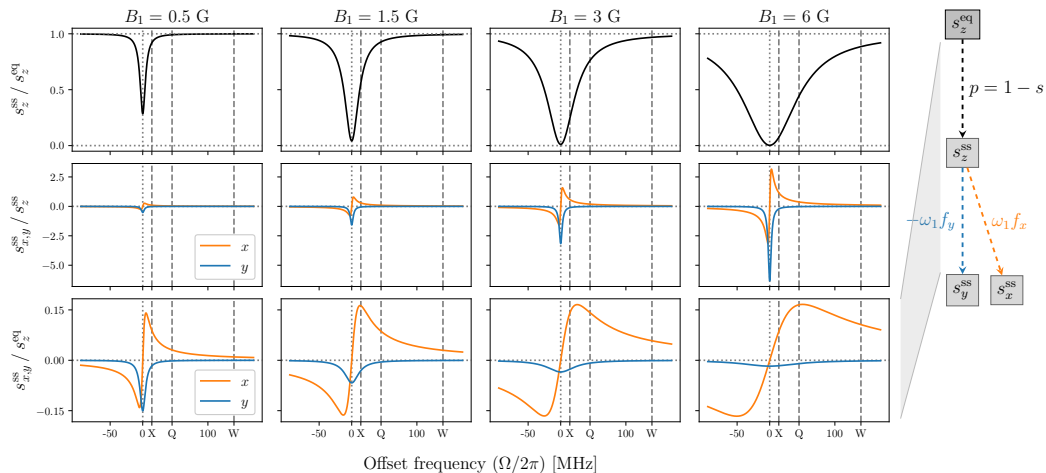


Figure 5. Transfer functions at-characterizing the steady state of the classical Bloch equations. The conversion of B_1 to ω_1 was for free radical with $g = 2$, hence $B_1 = 6$ G corresponds to $\omega_1/2\pi = 16.8$ MHz. In all plots $T_2 = 60$ ns and $T_1 = 9T_2$. The positions of the nuclear Larmor frequencies at X (14 MHz), Q (45 MHz) and W (140 MHz) bands are indicated with vertical dashed lines.

800 As our main interest is in the solid effect, we have indicated with dashed vertical lines the offsets Ω that correspond to the nuclear Larmor frequencies of a proton spin-proton Larmor frequencies at the X (9.2 GHz/14 MHz), Q (30 GHz/45 MHz) and W (92 GHz/140 MHz) mw bands. Considering that DNP is performed at high mw powers, let us examine the saturation at $B_1 = 6$ G (fig. 5, upper right plot).

Looking at $\Omega = \omega_I$ at X band, we see that the allowed EPR transition is almost completely saturated. Because the efficiency
 805 of the solid effect scales with $p = 1 - s$ (dashed orange arrow in fig p (eq. ??g(26)) any gain from efficiently driving the forbidden transitions will be squashed down dramatically, thus substantially reducing the ultimate enhancement of the NMR signal. This observation implies that at X band the best solid-effect enhancement may occur at less than maximum mw power, as we demonstrate numerically later in Sec. 6.2.

The second row of fig. 5 shows the offset dependence of the transfer functions connecting the longitudinal component s_z^{ss} to
 810 the transverse components $s_{x,y}^{ss}$. The observed increase in magnitude from left to right reflects the multiplication by ω_1 of the functions $f_{x,y}$ which are independent of ω_1 (eq. ~~These functions are~~(11)). Being the real (f_y) and imaginary (f_x) components of a complex-valued Lorentzian with width R_{2S} and center frequency $\Omega = 0$. In other words, they, these functions correspond to the absorptive and dispersive components of a homogeneous EPR line. The absorptive component (blue line) is largest at $\Omega = 0$, while the two extrema of the dispersive component (orange line) are located at $\Omega = \pm R_{2S}$. At offsets much larger than
 815 the locations of these extrema (i.e., $\Omega \gg R_{2S}$), the absorptive component drops as $1/\Omega^2$ while the dispersive component drops as $1/\Omega$.

The third row of fig. 5 shows the net transfer functions relating the outputs-input of the Bloch equations, $s_{x,y}^{ss}$, to the input s_z^{eq} . They s_z^{eq} to their ultimate outputs, $s_{x,y}^{ss}$. These transfer functions are obtained by multiplying the solid black lines in the

820 first row with the lines in the second row. In essence, what we see are the absorptive and dispersive components of a power-broadened EPR line. The power broadening (i.e., multiplication by $1 - s$) leads to qualitative differences. For example, while the peak of the blue line in the second row of the figure increased linearly with ω_1 , it now decreases as $1/\omega_1$. In the case of the orange line, the locations of its extrema are now shifted towards larger offsets ($\Omega \approx \pm \omega_1 \sqrt{T_{1S}/T_{2S}} \Omega \approx \pm \omega_1 (T_{1S}/T_{2S})^{1/2}$) and their magnitude is approximately independent of B_1 ($\approx \sqrt{T_{2S}/T_{1S}}/2 \approx 0.5(T_{2S}/T_{1S})^{1/2}$, which equals $1/6 \approx 0.17$ for the choice of relaxation times in fig. 5). Clearly, the tail of the power-broadened dispersive (orange) component extends further

825 into the range of interest for the solid effect at high mw frequencies than the tail of the absorptive (blue) component. One could thus expect that the path through s_x^{SS} contributes to the solid effect more than in fig. 3a (orange arrows) contributes to v_- more than the path through s_y^{SS} (blue arrows), simply because the latter s_y^{SS} does not survive at offsets equal to the nuclear Larmor frequencies at high fields. This observation is in line with the decision of Erb, Motehane and Uebersfeld to drop the term proportional to s_y when arriving at (Erb et al., 1958a).

830 The functions in the second row of fig. 5 were depicted as the even and odd components of the first filter in fig. 10. In fact, we should have shown the power-broadened versions of these functions (third row of fig. 5). The peak of the solid blue line in fig. 10 would then be substantially reduced at high mw powers, providing additional reason for the absence of the solid effect in the vicinity of ω_S . In contrast, the peak of the dashed blue line is not reduced with power but only moves away from the EPR resonance position, without compromising the possibility of solid-effect DNP enhancement at the “wrong” offset which

835 corresponds to the blue star in fig. 10.

5.2 ~~Steady state of the coupled~~ Generalized Bloch equations

We now proceed to the analysis of the two coupled Bloch equations from fig. 2d. Our goal is to compare their steady state with fig. 2c and thus identify the forbidden transition rates v_{\pm} . Because we already determined the electronic steady state, the problem we need to solve looks like shown in fig. ??a.

840 In this figure, the outputs $s_{x,y}^{SS}$ of the first set of Bloch equations serve as inputs to the second set of Bloch equations. This second set (enclosed in a dashed rectangle in fig. ??a) constitutes the dynamical system whose steady-state response we aim to characterize. In addition to the two inputs mentioned above, this system takes a third input (i_z) and produces the output that comes out of the red arrow. Our task is to determine the relationship between the three inputs and the output of this system at steady state.

845 The steady-state solution of is

$$\begin{bmatrix} g_x^{SS} \\ g_y^{SS} \\ g_z^{SS} \end{bmatrix} = -i \frac{1}{4} A_1 \mathcal{B}^{-1} \begin{bmatrix} -i s_y^{SS} \\ i s_x^{SS} \\ i_z^{SS} \end{bmatrix}.$$

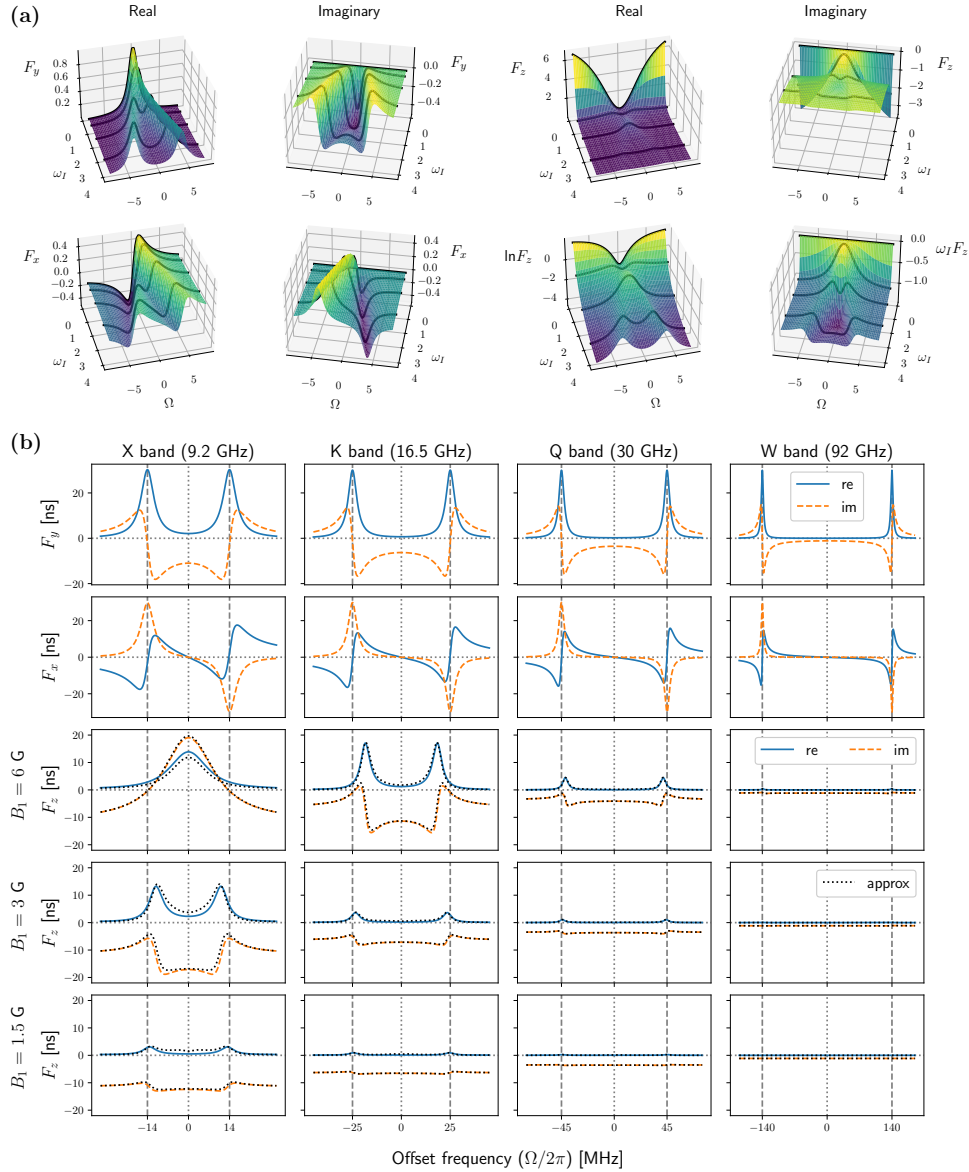


Figure 6. The functions F_y , F_x and F_z characterizing the steady state of the second set of Bloch equations. **(a)** Angular frequencies are measured in units of R_{2S} . $R_{1S} = R_{2S}/9$ as in the other figures. To calculate F_z we used $\omega_1 = 1.5$, which for $T_{2S} = 60$ ns corresponds to $B_1 \approx 1.5$ G. Solid black lines are cross-sections at $\omega_I = 0, 0.5, 1.5, 3$. **(b)** Numerical parameters as in fig. 5. Recall that $B_1 = 6$ G corresponds to $\omega_1/2\pi = 16.8$ MHz.

Because only g_z^{ss} feeds into the time derivative of i_z (eq.), we have

$$\dot{i}_z|_{\text{coh}}^{\text{ss}} = -\delta^2 \text{Re} \left\{ \begin{bmatrix} 0 & 0 & 1 \end{bmatrix} \mathcal{B}^{-1} \begin{bmatrix} -i s_y^{\text{ss}} \\ i s_x^{\text{ss}} \\ i_z^{\text{ss}} \end{bmatrix} \right\},$$

where the dipolar coupling was factored out as

$$850 \quad \delta^2 = (A_1^* A_1)/4.$$

Clearly, the output is a linear combination of the three inputs and can be written as

$$\dot{i}_z|_{\text{coh}}^{\text{ss}} = -\delta^2 (T_{ix} s_x^{\text{ss}} + T_{iy} s_y^{\text{ss}} + T_{ii} i_z^{\text{ss}}),$$

which is illustrated [Numerical parameters as in fig. ??b](#). Since δ has units of inverse time, the transfer functions T_{in} ($n = x, y, i$) must have units of time. Comparing and, we see that

$$855 \quad \begin{aligned} T_{iy} &= \text{Re}\{-i\mathcal{B}_{31}^{-1}\}, & T_{ix} &= \text{Re}\{i\mathcal{B}_{32}^{-1}\} \\ T_{ii} &= \text{Re}\{\mathcal{B}_{33}^{-1}\}, \end{aligned}$$

where \mathcal{B}_{ij}^{-1} is the ij th element of the matrix \mathcal{B}^{-1} .

The needed matrix elements in the last row of \mathcal{B}^{-1} can be obtained from the cofactors of the last column of \mathcal{B} as follows:-

$$\begin{aligned} \mathcal{B}_{31}^{-1} &= \omega_1 \Omega / \Delta, & \mathcal{B}_{32}^{-1} &= \omega_1 (R_{2S} + i\omega_I) / \Delta \\ \mathcal{B}_{33}^{-1} &= [(R_{2S} + i\omega_I)^2 + \Omega^2] / \Delta, \end{aligned}$$

where the determinant of \mathcal{B} is

$$860 \quad \Delta = (R_{1S} + i\omega_I)[(R_{2S} + i\omega_I)^2 + \Omega^2] + \omega_1^2 (R_{2S} + i\omega_I).$$

5.2.1 Characterizing the second set of Bloch equations

Let us now introduce the complex-valued functions-

$$\begin{aligned} F_y &= \frac{1}{R_{2S} + i\omega_I + \Omega \frac{1}{R_{2S} + i\omega_I} \Omega} \\ F_x &= \frac{\Omega}{R_{2S} + i\omega_I} F_y, & H &= \frac{1}{R_{1S} + i\omega_I + \omega_1 F_y \omega_1}, \end{aligned}$$

which generalize the functions of the classical Bloch equations by supplementing their relaxation rates with an imaginary part.

865 Like their classical analogs, these functions have units of time (Table 1). In terms of them, the matrix elements can be rewritten as-

$$\mathcal{B}_{31}^{-1} = \omega_1 F_x H, \quad \mathcal{B}_{32}^{-1} = \omega_1 F_y H, \quad \mathcal{B}_{33}^{-1} = H.$$

Then, using, we express the three transfer functions of interest (fig. ??b) as-

$$\underline{T_{ix,y} = \pm \omega_1 \text{Re}\{i F_{y,x} H\}}, \quad T_{ii} = \text{Re}\{H\}.$$

870 ~~Because all steady-state properties of the second set of Bloch equations (inside the dashed rectangle in fig. [The transfer functions indicated with colored arrows in fig. \[??a\]\(#\)](#)~~ are contained in the functions F_x, F_y and F_z (eq. (48)), let us examine them more closely. [4b](#) depend on the auxiliary functions F_x, F_y and F_z (eq. (48)). These three complex-valued functions are plotted in the ω_I - Ω plane in fig. [??6a](#). In ~~these the~~ plots, the angular frequencies are reported in units of R_{2S} . Cross-sections at $\omega_I = 0, 0.5, 1.5, 3$ are drawn over the surfaces with solid black lines.

875 The black lines at $\omega_I = 0$ show that the imaginary parts of ~~the functions~~ F_y, F_x and ~~H vanish~~ F_z vanish, and their real parts become equal to f_y, f_x and ~~h~~ f_z of the classical Bloch equations (cf. fig. 5, first two rows). In particular, at $\omega_I = 0$, F_y and F_x as functions of Ω are like the absorptive and dispersive components of the EPR line. ~~To plot the function H~~ ~~When plotting F_z~~ we used $\omega_1 = 1.5$ (in units of R_{2S}). Because both the real and imaginary parts of ~~H~~ F_z decay very rapidly with increasing ω_I , we also show the logarithm of the real part and the product of the imaginary part with ω_I . These transformations make visible

880 the small values ~~of F_z~~ at large ω_I .

In fig. [??6b](#) we show these functions against Ω at four different nuclear Larmor frequencies and, in the case of ~~H~~ F_z , three different mw powers. In each case, the locations of the Larmor frequencies along the horizontal axis are indicated with vertical dashed lines. In the first and second rows we see F_y and F_x , which do not change with mw power. The real and imaginary parts of F_y (first row) look like the real and imaginary parts of two complex-valued Lorentzians centered at $\Omega = -\omega_I$ and $\Omega = +\omega_I$.

885 Indeed, with

$$L_{\pm} = [R_{2S} + i(\omega_I \pm \Omega)]^{-1}, \quad (50)$$

it is straightforward to show that $F_y = (L_- + L_+)/2$. These Lorentzians have the same width as f_y and f_x of the classical Bloch equations (fig. 5, second row). The function F_x in the second row of fig. [??6b](#) also has Lorentzian-like features centered at $\Omega = \pm\omega_I$, but the Lorentzian on the right is flipped around the horizontal axis. Indeed, it can be shown that $F_x = (L_- - L_+)/2$.

890 Differently from $F_{x,y}$, ~~H~~ F_z depends on ω_1 (eq. (40)). In the last three rows of fig. [??6b](#) we plot ~~$H(\Omega)$~~ $F_z(\Omega)$ for three different values of B_1 , starting with $B_1 = 6$ G (third row) and going down to $B_1 = 1.5$ G (last row). The first thing to notice is that both the real (blue) and imaginary (orange) parts of this function decrease rapidly with increasing ω_I , i.e., moving to the right in a given row. (The former as $1/\omega_I^2$ and the latter as $1/\omega_I$.) As all transfer functions (48) are proportional to ~~H~~ F_z , we expect these to also decrease rapidly with increasing nuclear Larmor frequency.

895 At the lower mw powers and higher magnetic fields ~~H~~ F_z is seen to be dominated by its imaginary part, as its real part remains close to zero. At higher mw powers and lower magnetic fields ($B_1 = 6$ G, X and K bands, and $B_1 = 3$ G, X band) the real and imaginary parts are seen to be comparable in magnitude. Moving from the former to the latter regime, there is a major qualitative change: the features at $\Omega = \pm\omega_I$ shift towards the origin ($B_1 = 6$ G, K band, and $B_1 = 3$ G, X band) until they coalesce into a single line ($B_1 = 6$ G, X band).

900 In Paper II we calculate ~~the inverse of the matrix~~ \mathcal{B} F_z approximately using perturbation theory. ~~The matrix element~~ $\mathcal{B}_{33}^{-1} = H$ is found to be

$$H \approx \frac{\cos^2 \alpha}{\tilde{R}_1 + i\omega_I} + \frac{\frac{1}{2} \sin^2 \alpha}{\tilde{R}_2 + i(\omega_I - \omega_{\text{eff}})} + \frac{\frac{1}{2} \sin^2 \alpha}{\tilde{R}_2 + i(\omega_I + \omega_{\text{eff}})},$$

, and find

$$F_z \approx \frac{\cos^2 \alpha}{\tilde{R}_1 + i\omega_I} + \frac{\frac{1}{2} \sin^2 \alpha}{\tilde{R}_2 + i(\omega_I - \omega_{\text{eff}})} + \frac{\frac{1}{2} \sin^2 \alpha}{\tilde{R}_2 + i(\omega_I + \omega_{\text{eff}})}, \quad (51)$$

905 where the frequency $\omega_{\text{eff}} = \sqrt{\Omega^2 + \omega_I^2}$, $\omega_{\text{eff}} = (\Omega^2 + \omega_I^2)^{1/2}$ corresponds to the effective magnetic field, α is the angle between this field and B_0 ($\cos \alpha = \Omega/\omega_{\text{eff}}$, such that $\cos \alpha = \Omega/\omega_{\text{eff}}$ and $\sin \alpha = \omega_I/\omega_{\text{eff}}$), and

$$\begin{aligned} \tilde{R}_1 &= R_{1S}(\cos \alpha)^2 + R_{2S}(\sin \alpha)^2 \\ \tilde{R}_2 &= R_{2S}[1 - (\sin \alpha)^2/2] + R_{1S}(\sin \alpha)^2/2. \end{aligned} \quad (52)$$

This result is exact for $R_{1S} = R_{2S}$ and is perturbative in the difference of the two electronic relaxation rates (Sezer, 2023).

The approximation (51) is shown with dotted black lines in the last three rows of fig. ??6b. It is seen to correctly capture both
 910 the shift of the peaks towards smaller offsets and their coalescence at $\Omega = 0$. Inspecting (51) we see that the dependence of H
 F_z on Ω is in the form of two Lorentzians centered at $\omega_{\text{eff}} = \pm\omega_I$, which implies $\Omega^2 = \omega_I^2 - \omega_{\text{eff}}^2$ comes from the second and
 third summands. The second summand is a complex-valued Lorentzian centered at $\omega_{\text{eff}} = \omega_I$, which corresponds to the offsets
 $\Omega = \pm(\omega_I^2 - \omega_{\text{eff}}^2)^{1/2}$. This explains the deviation of the maxima from the canonical solid-effect positions $\Omega = \pm\omega_I$ for $\omega_1 \approx \omega_I$.
 At X band, when $B_1 = 6$ G, ω_1 is larger than ω_I and the two Lorentzians fuse together. It is noteworthy that the equality
 915 $\omega_{\text{eff}} = \omega_I$, implied by the approximation (51), also arises as the matching condition of the pulsed DNP method known as
 NOVEL (nuclear orientation via electron spin locking) (Henstra et al., 1988; Henstra and Wenckebach, 2008; Jain et al., 2017).

5.2.1 Combining the two sets of Bloch equations

Having examined the functions $F_{x,y}$ and H , we now turn to the transfer functions, which are indicated (48), which were
 920 depicted with colored arrows in fig. ??4b. These are plotted in the second and third rows of fig. ??:

Transfer functions at the steady state of the coupled Bloch equations. $B_1 = 6$ G, $T_{2S} = 60$ ns and $T_{1S} = 9T_{2S}$.

As T_{ii} . As T_i (solid red lines) is just the real part of $H F_z$, it exhibits all the features that we already talked about when
 discussing fig. ??b. Although, in principle, T_{ii} corresponds to the rate v_+ , it accounts for both the two-step and four-step loops
 that we observed in 6b. The dashed red lines in the third row of fig. 2d. The former corresponds to the 7 correspond to the
 925 mw-independent part of T_i , namely $T_i^0 = T_i(\omega_1 = 0)$, which contributes to the nuclear relaxation rate w_1 in fig. ??b, and is
 already included in R_{1T} . Hence its contribution has to be removed when identifying rather than to v_+ .

Since the nuclear T_1 is typically measured with the microwaves switched off, we identify

$$T_{ii}^0 = \text{Re}\{H(\omega_1 = 0)\} = \text{Re}\{(R_{1S} + i\omega_1)^{-1}\}$$

as contributing to relaxation. Subtracting it from T_{ii} , we deduce

$$930 \quad v_+/\delta^2 = T_{ii} - T_{ii}^0 = \text{Re}\{H - (R_{1S} + i\omega_1)^{-1}\}.$$

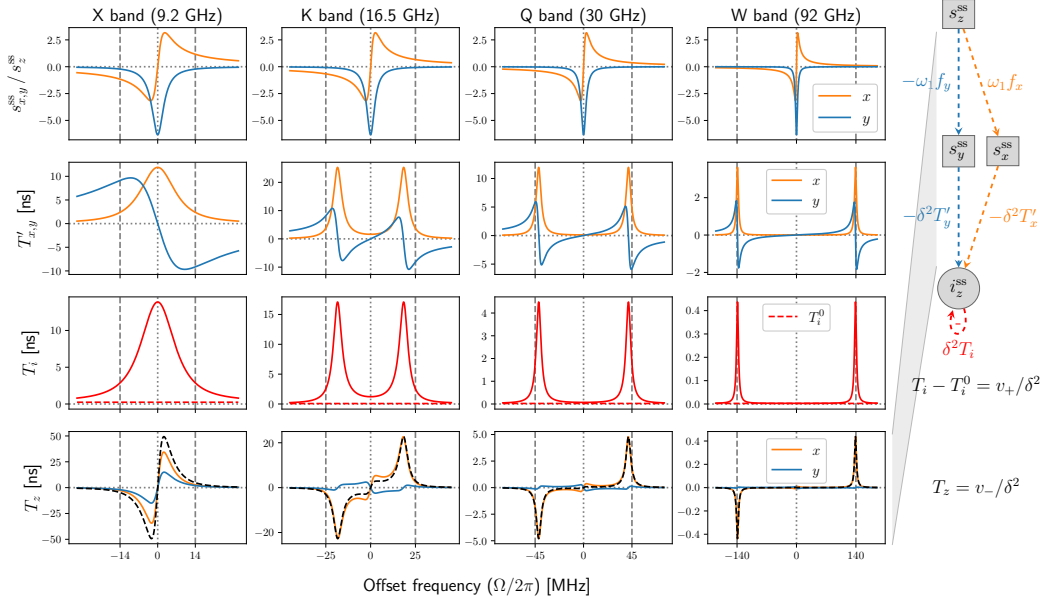


Figure 7. Transfer functions characterizing the steady state of the two coupled sets of Bloch equations. Used parameters: $B_1 = 6$ G, $T_{2S} = 60$ ns and $T_{1S} = 9T_{2S}$.

T_{ii}^0 is plotted with red dashed lines in the third row of fig. (eq. ??(47)). At the high mw field that we have used ($B_1 = 6$ G) it, T_{ii}^0 is negligible compared to T_{ii} itself T_{ii} (solid red line), thus subtracting the relaxation would not make much of a difference. However, at lower mw powers the contribution of $T_{ii} T_{ii}$ to thermal relaxation becomes comparable to the rest, and the correction makes a difference. (This can be seen in the bottom plot of fig. A1 where $B_1 = 1$ G.)

935 In the second row of fig. ??7, the functions $T_{i,x,y} T'_{x,y}$ resulted from the product of $F_{y,x}$ and $H F_z$ (eq. (48)). Interestingly, their Lorentzian-like features are at the same frequency offsets as those of $T_{ii} T_{ii}$, the real part of H . (The functions $T_{i,x,y}$ were shown in fig. 10 as the even and odd components of the second filter). F_z . We observe that $T_{i,x} T'_x$ (orange) and $T_{i,y} T'_y$ (blue) are similar in magnitude. Thus, if the inputs s_x^{ss} and s_y^{ss} were comparable in magnitude, the contributions of the two parallel branches from s_z^{ss} to the output i_z^{ss} would be similar (see flow diagram in the right margin of fig. ??7). We know, however, that

940 s_y^{ss} is much smaller than s_x^{ss} at large offsets (fig. 7, first row), and so the path via $T_{i,x} T'_x$ (orange) will contribute more.

To determine the rate v_- , which connects s_z to the time derivative of i_z at steady state (fig. ??c), we should treat s_z^{ss} as an input (not $s_{x,y}^{ss}$). Multiplying the functions $T_{i,x,y} T'_{x,y}$ (fig. ??7, second row) by the functions in the first row, we obtain the orange and blue lines in the last row of the figure. (The functions in the first row were shown before in fig. 5. They are plotted here again only for $B_1 = 6$ G. The four plots are identical to each other but appear different due to the different scales of the

945 horizontal axes.) Comparing the first and second rows of fig. ??7, we see that an odd/even function in the first row is multiplied by an even/odd function in the second row to produce the corresponding orange and blue lines in the bottom row. As a result, the contribution of both parallel paths from s_z^{ss} to i_z^{ss} (via either s_x^{ss} or s_y^{ss}) is odd in Ω .

The cumulative transfer function of the two parallel paths is obtained by adding the orange and blue lines in the last row of fig. ???. It equals (compare fig. ??b and fig. ??e)

$$950 \quad T_{iz} = \omega_1 f_x T_{ix} - \omega_1 f_y T_{iy} = v_- / \delta^2,$$

and (49)) is also plotted in the last row of fig. ??? with black dashed lines.

As already mentioned in the introduction, this cumulative transfer function results from two band-pass filters connected in series and centered at $\Omega = 0$ (fig. ??, top row) and at $\Omega \approx \pm \omega_I$ (fig. ??, second row). The composite filter (fig. ??, bottom row) will only “pass a signal” to the extent that the tails of the “dispersive” component of one of the filters and the “absorptive” component of the other filter overlap. When this overlap is small, the corresponding transitions are “forbidden”.

At Q and W bands the cumulative transfer function (fig. ??, bottom row, black dashed lines) it is seen to be essentially identical to its first additive contribution $\omega_1 f_x T_{ix}$ (orange line), which means that the electronic polarization is transferred to the nucleus almost entirely through the dispersive component s_x^{SS} . This conclusion supports the assumption of Erb, Motchane and Uebersfeld (Erb et al., 1958a).

960 From and we have

$$T_{iz} = \omega_1^2 \text{Re}\{i(f_x F_y + f_y F_x)H\}.$$

Incidentally,

$$f_x F_y + f_y F_x = f_x F_y \frac{2R_{2S} + i\omega_I}{R_{2S} + i\omega_I} = f_x F'_y,$$

In the light of this observation, we will now rewrite the cumulative transfer function T_z (eq. (49)) as if the polarization was transferred only through the dispersive component. We start by observing that

$$965 \quad F_y f_x + F_x f_y = F_y \frac{2R_{2S} + i\omega_I}{R_{2S} + i\omega_I} f_x = F'_y f_x, \quad (53)$$

where the last equality defines F'_y . The second R_{2S} in the numerator of (53) comes from $f_y F_x - F_x f_y$ and can be viewed as a “correction” to $f_x F_y$ due to $f_y F_x$. The last row of fig. ??? already demonstrated that this correction becomes negligible at increasingly large nuclear Larmor frequencies. Here we see this analytically.

970 Using the cumulative transfer function from s_z^{SS} to i_z^{SS} can be expressed as if there was only one path through s_x^{SS} , as illustrated in fig. ???d. In other words, it is possible to rewrite exactly, $F_y f_x$ due to $F_x f_y$. Introducing

$$T_x = \text{Re}\{iF_z(\omega_1 F'_y)\}, \quad (54)$$

(compare this T_x with T'_x in (48)), we rewrite (42) in a way that contains s_x^{SS} but does not contain s_y^{SS} :

$$i_z|_{\text{coh}}^{SS} = -\delta^2 (T'_{ix} s_x^{SS} + T_{ii} i_z^{SS}),$$

975 ~~with~~

$$\underline{T'_{ix} = \omega_1 \text{Re}\{iF'_y H\}}.$$

(Compare this T'_{ix} with T_{ix} in eq. (42).) Hence, the phenomenological equation of Erb, Motchane and Uebersfeld is, in fact, exact with $\nu = -\delta^2 T'_{ix}$ as follows:

$$\dot{i}_z|_{\text{coh}}^{\text{ss}} = -(\delta^2 T'_i) i_z^{\text{ss}} - (\delta^2 T_x) s_x^{\text{ss}}. \quad (55)$$

980 Note that this expression is exact, and does not result from simply dropping the last term in (42), which is proportional to s_y^{ss} , as the contribution of the path through s_y^{ss} is taken into account in the definition of T_x .

In summary, we derived the following exact expressions for the rate constants of the forbidden transitions:

$$\underline{v_+ = \delta^2 (T_{ii} - T_{ii}^0), \quad v_- = \delta^2 T_{iz} = \delta^2 (\omega_1 f_x) T'_{ix}}.$$

Equation (55) is depicted in fig. 4d, which shows only one path from s_z^{ss} to i_z^{ss} going through s_x^{ss} . From fig. 4d,

$$985 \quad \underline{v_- = (\omega_1 f_x) (\delta^2 T_x)}. \quad (56)$$

This factorization is revisited in Sec. 7.1.

6 Use of Closer look at the rate constants

6.1 Relation to the classical rates

990 ~~Now Here~~ we show that the classical expression of the ZQ and DQ transition rates (eq. (28)) follows from the exact rates (eqs. (47) and (56)) when $\omega_1 \ll \omega_I$.

To simplify the analysis, we take from the start a long electronic T_1 relaxation time, such that $R_{1S} \ll \omega_I$. This should be the case under solid-effect DNP conditions for high-field DNP in solids, where the electronic T_1 is at least a microsecond. In this case the function H (eq. (40)) simplifies to

$$\underline{H \approx \frac{1}{i\omega_I + \omega_1^2 F_y} = \frac{1}{i\omega_I} \left(1 + \frac{\omega_1^2}{i\omega_I} F_y\right)^{-1}}.$$

995

$$\underline{F_z \approx \frac{1}{i\omega_I + \omega_1^2 F_y} = \frac{1}{i\omega_I} \left(1 + \frac{\omega_1^2}{i\omega_I} F_y\right)^{-1}}. \quad (57)$$

For $\omega_1 \ll \omega_I$, to first order in ω_1^2 ,

$$\underline{H \approx \frac{1}{i\omega_I} + \frac{\omega_1^2}{\omega_I^2} F_y}.$$

From

$$1000 \quad F_z \approx \frac{1}{i\omega_I} + \frac{\omega_1^2}{\omega_I^2} F_y. \quad (58)$$

Note that, because the relaxation rate R_{1S} was neglected, $T_i^0 = \text{Re}\{F_z(\omega_1 = 0)\} = 0$. In other words, the contribution of the short path in fig. 3b (blue and red arrow) to the nuclear relaxation rate vanishes. From (47) and (56), retaining only terms of up to first order in ω_1^2 ,

$$v_+ \approx \delta^2 \frac{\omega_1^2}{\omega_I^2} \text{Re}\{F_y\}, \quad v_- \approx \delta^2 \frac{\omega_1^2}{\omega_I^2} \omega_I f_x \text{Re}\{F'_y\}.$$

1005

$$v_+ \approx \delta^2 \frac{\omega_1^2}{\omega_I^2} \text{Re}\{F_y\}, \quad v_- \approx \delta^2 \frac{\omega_1^2}{\omega_I^2} \omega_I f_x \text{Re}\{F_y \frac{2R_{2S} + i\omega_I}{R_{2S} + i\omega_I}\}. \quad (59)$$

To establish the equivalence of these expressions with (28), we need to show that $\text{Re}\{F_y\}$ and $\omega_I f_x \text{Re}\{F'_y\}$ equal, respectively, the sum and difference of two real-valued Lorentzians centered at $\Omega = \pm\omega_I$. For the complex-valued Lorentzians (50), we already observed that $L_- + L_+ = 2F_y$. One can also confirm that $\text{Re}\{L_- - L_+\} = 2\omega_I f_x \text{Re}\{F'_y\}$. Hence,

$$1010 \quad v_{\pm} \approx \frac{1}{2} \delta^2 \frac{\omega_1^2}{\omega_I^2} (\text{Re}\{L_-\} \pm \text{Re}\{L_+\}),$$

and thus

$$v_{0,2} \approx \frac{1}{8} (A_1^* A_1) \left(\frac{\omega_1}{\omega_I}\right)^2 \text{Re}\{L_{\pm}\},$$

$$v_{\pm} \approx \delta^2 \frac{\omega_1^2}{\omega_I^2} \frac{1}{2} (\text{Re}\{L_-\} \pm \text{Re}\{L_+\}), \quad (60)$$

1015 and thus

$$v_{0,2} \approx \frac{1}{8} (A_1^* A_1) \frac{\omega_1^2}{\omega_I^2} \text{Re}\{L_{\pm}\}, \quad (61)$$

which is the classical result (28).

The sum and difference of the classical rates v_2 and v_0 is compared with the exact v_{\pm} in the first two rows of fig. 8. Naturally, the Lorentzians associated with the classical rates remain centered at $\pm\omega_I$ even when the maxima of the exact rates shift closer to each other at Q and K bands, and converge at X band. At high fields (e.g. W band), where $\omega_I \gg \omega_1$, the classical approximations work perfectly.

In the last row of fig. 8 we show the DQ-transition rate v_2 . While, classically, it is always non-negative (black dashed lines), the exact rate deduced from v_{\pm} (solid brown lines) is seen to become negative at some offsets. From the perspective of the rate-equation formalism, such negative rates are meaningless. In that sense, the description of the forbidden transitions in terms of v_{\pm} is more fundamental than their description in terms of v_0 and v_2 .

1025

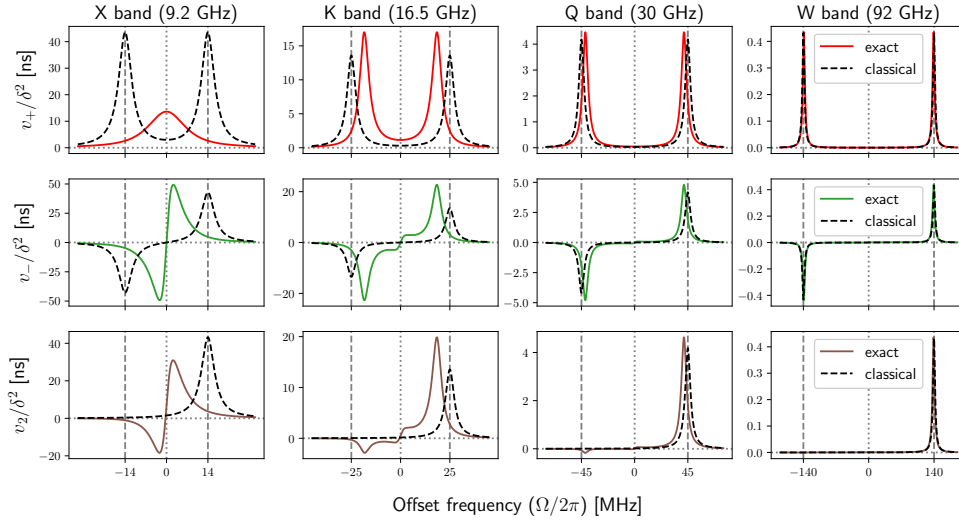


Figure 8. Forbidden-transition rates calculated either exactly (solid lines) or using the classical expression (28) with $v_{\pm} = v_2 \pm v_0$ (dashed lines). As in the previous figures, $B_1 = 6$ G, $T_{2S} = 60$ ns and $T_{1S} = 9T_{2S}$.

6.2 Solid-effect DNP enhancement

The DNP enhancement of the solid effect (eq. (26)) was can be written as the product of $|\gamma_S|/\gamma_I$ with the following two **factors**:

$$pX = \frac{R_{1I}/\delta^2}{R_{1I}/\delta^2 + (T_{ii} - T_{ii}^0)}, \quad pv_- = \frac{pT_{iz}}{R_{1I}/\delta^2},$$

1030 dimensionless factors:

$$pX = \frac{R_{1I}/\delta^2}{R_{1I}/\delta^2 + (T_i - T_i^0)}, \quad pv_- = \frac{pT_z}{R_{1I}/\delta^2}, \quad (62)$$

which we have rewritten here in terms of the transfer functions T_{ii}, T_{ii}^0 and T_{iz}, T_i, T_i^0 and T_z . These transfer functions already appeared in the last two rows of fig. ???. Thus, to calculate the DNP enhancement, we only need to specify the ratio R_{1I}/δ^2 .

In the case of δ , rather than calculating A_1 (eq. (30)) for some arbitrary inter-spin vector, let us average $A_1^* A_1$ over the entire
 1035 3D space. With b denoting the so called ‘‘distance of closest approach’’ or ‘‘contact distance’’, and N denoting the number of electron spins per unit volume, we have

$$\langle \delta^2 \rangle = \frac{1}{4} \langle A_1^* A_1 \rangle = D_{\text{dip}}^2 \frac{6\pi}{5} \frac{N}{3b^3}, \quad (63)$$

where, in this case, the angular brackets denote spatial averaging. We will use $b = 1$ nm and $N = 0.1$ M as representative, but otherwise arbitrary values.

1040 While the average over 3D space in (63) is clear mathematically, it is important to understand that physically it implies fast spin diffusion (Wind et al., 1985). Since the nuclear polarization in solids is homogenized across the sample through spin

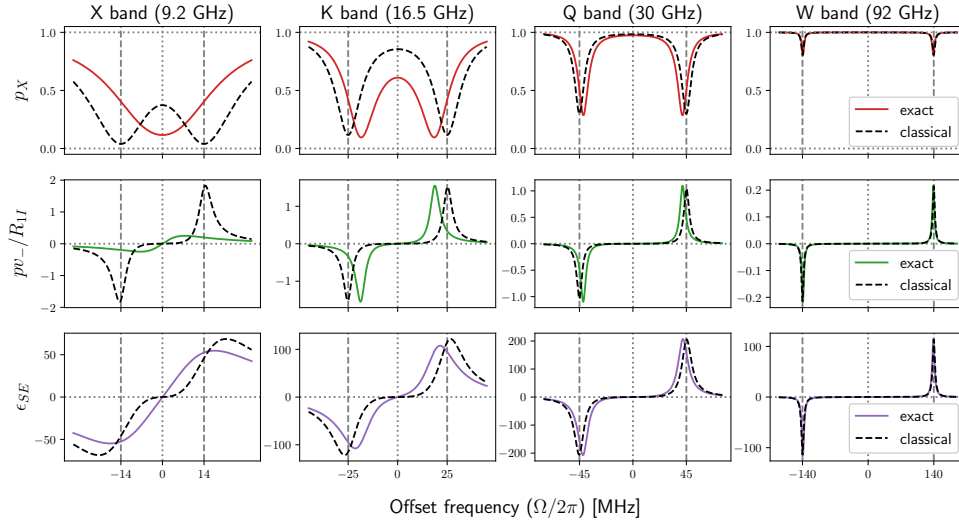


Figure 9. Decomposition of the DNP field profile (ϵ_{SE}) in terms of the multiplicative contributions p_X and p_{v-}/R_{1I} . The new parameters used here are $T_{1I} = 30$ ms, $b = 1$ nm and $N = 0.1$ M. Other parameters: $B_1 = 6$ G, $T_{2S} = 60$ ns and $T_{1S} = 9T_{2S}$.

diffusion, replacing the individual δ^2 's of the nuclear spins by the average over all nuclei is only legitimate when spin diffusion is faster than the nuclear spin-lattice relaxation. In practice, spin diffusion is rather slow and is often the bottleneck for efficient polarization transfer in solids (Hovav et al., 2011; Smith et al., 2012; Pinon, 2018). As a result, the DNP enhancement values that we will calculate with (63) are expected to be appreciably larger than what could be observed experimentally.

Similar considerations also apply for the choice of the nuclear spin-lattice relaxation time. In principle T_{1I} will depend on the distance of the nucleus from the electronic spin, and thus will vary greatly across the sample. In the limit of fast spin diffusion, however, only its average value becomes relevant. In general, this time depends on the radical concentration and on the magnetic field B_0 . However, for the purposes of illustration, here we take a generic numerical value of $T_{1I} = 30$ ms across all mw bands. Again, this value is realistic but otherwise arbitrary.

Using $b = 1$ nm, $N = 0.1$ M and $T_{1I} = 30$ ms we find $R_{1I}/\langle\delta^2\rangle = 1.78$ ns. Let us visually compare this time scale with $(T_{ii} - T_{ii}^0) = v_+ / \langle\delta^2\rangle \cdot (T_i - T_i^0) = v_+ / \langle\delta^2\rangle$ by consulting the solid red line in the first row of fig. 8. We observe that at X and K bands the maxima of the red line are much larger than 2 ns, which means that the minima of p_X will be close to zero. At Q band the maxima of the red line are comparable to 2 ns, and at W band they are much smaller. The minima of the nuclear cross-polarization factor are thus expected to be about one half and one, respectively. These expectations are confirmed by the maroon lines in the first row of fig. 9, which demonstrate that the ratio p_X can substantially deviate from one at lower magnetic fields.

To estimate the expected magnitude of the second factor in (62), we need to compare the time scale $R_{1I}/\langle\delta^2\rangle = 1.78$ ns with pT_{iz} . While $T_{iz} pT_{iz}$ was shown with black dashed lines in the bottom row of fig. ??7, now it has to be multiplied by the electronic polarization factor in the top row of fig. 5. From the line for $B_1 = 6$ G in this row, we see that $T_{iz} T_{iz}$ will be

significantly suppressed at X band, so it is hard to judge how the reduced value will compare with 1.78 ns. At Q band, $T_{iz}T_z$ will be reduced by a little more than a factor of two, which will make its peak in fig. ?? comparable to $R_{1I}/\langle\delta^2\rangle$. At W band, where the factor p is about 0.9, $T_{iz}T_z$ will be only slightly reduced, so its peak is expected to be about one fifth of 1.78 ns. Again, these estimates are confirmed by the green lines in the second row of fig. 9.

1065 The last row of fig. 9 shows the product of the first two rows times $|\gamma_S|/\gamma_I$, assuming a proton spin. The result is the solid-effect DNP enhancement (eq. (26)). In the figure we have also shown the factors predicted by the classical expression of the rates (eq. (28)) with black dashed lines. While there are quantitative differences between the exact calculations and the classical approximation, the magnitudes of the DNP enhancements in the two cases are, in fact, comparable. A closer look reveals that, for the specific B_1 and relaxation times used in the calculations, the classical description of the solid effect (eq. (28)) works
 1070 perfectly at Q band and at larger mw frequencies. (In fig. A2 we show that by reducing the mw power to $B_1 = 1$ G the classical expressions are also perfect at X band.) The amplitudes of the maximum enhancements at the four mw bands are roughly in the ratios 1 : 2 : 4 : 2 (X:K:Q:W). On the other hand, considering the inverse dependence on ω_I^2 , we expect the ratios 100 : 40 : 10 : 1. These expected ratios are indeed observed at the much lower mw power of $B_1 = 1$ G (fig. A2, lower plot). Comparison of figs. 9 and A2, shows that increasing B_1 increases the amplitudes of the maximum enhancements at W and Q bands, but reduces
 1075 the enhancement at X band. Such reduction of the solid-effect DNP enhancement with increasing B_1 has been reported at X band (Neudert et al., 2016).

7 ~~Conclusion~~ Concluding discussion

~~In this paper we presented a way of thinking about~~

7.1 Refactorization of the polarization transfer

1080 When $p_X \approx 1$ (eq. (26)), e.g., at high magnetic fields (fig. 9, W band) and lower mw powers (fig. A2, lower half), the DNP enhancement of the solid effect ~~which was grounded in the dynamics of the spins is~~

$$\epsilon_{SE} \approx (pv_-)T_{1I}|\gamma_S|/\gamma_I \quad (p_X \approx 1). \quad (64)$$

Since T_{1I} is easily accessible experimentally, pv_- is the only non-trivial factor in (64). From fig. 4a we know that p relates s_z at steady state to s_z^{eq} , and from fig. 4c we know that v_- relates the time derivative of i_z at steady state ~~The spin dynamics of the four-level system that we analyzed requires only 16 different spin operators, including the identity operator. It is thus completely described by a 16×16 propagation matrix in Liouville space, and can be simulated numerically using a spin-dynamics simulation package (Bengs and Levitt, 2018; Yang et al., 2022). Such numerical simulations would provide answers to many specific questions, including the efficiency of the solid effect for the parameters that we explored here. Nevertheless, having an intuitive understanding of the spin dynamics which is relevant for a given phenomenon is invaluable to s_z . Hence, the product~~
 1090 pv_- relates the time derivative of i_z directly to the electronic Boltzmann polarization s_z^{eq} , as shown graphically in the left half of fig. 10.

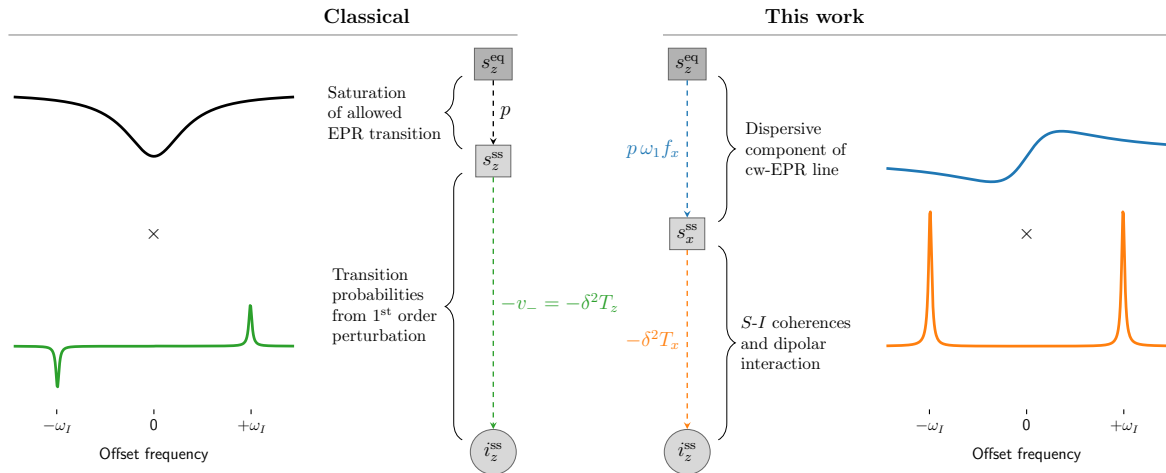


Figure 10. Two ways of decomposing the effect of the electronic Boltzmann polarization (s_z^{eq}) on the steady-state nuclear polarization (i_z^{ss}). The classical way (left) partitions this effect into the factors p and $v_- = v_2 - v_0$, which reflect respectively the saturation of the allowed EPR transition and the excitation of the forbidden DQ (v_2) and ZQ (v_0) transitions. Alternatively (right), the same effect can be written as the product of the dispersive component of the power-broadened EPR line ($s_x^{\text{ss}}/s_z^{\text{eq}}$) and the rate constant $\delta^2 T_x$. The latter characterizes the steady state of the electron-nucleus coherences without any contribution from the purely electronic coherences.

Here, we followed a systematic procedure for deriving the relevant equations of motion under a given spin Hamiltonian (See Since, by construction, the rate equations of the polarizations do not model the dynamics of the coherences, their steady state balances the rates of mw excitation only against the longitudinal (i.e., spin-lattice) relaxations. The polarization factor p quantifies this balance for the allowed EPR transition (eq. ??), and developed a graphical representation to visualize the interplay of these equations ((3)). Because the rate equations work only with the polarizations, all dynamical variables between s_z and i_z in fig. 2d). While our analysis focused on the solid effect and the Hamiltonian, it should be possible to analyze other related effects with different Hamiltonians in a similar way. In any case, for a four-level system the resulting dynamics will comprise at most fifteen coupled differential equations. Here, we explicitly considered the dynamics of seven spin operators are

1095

1100

lumped into the rate constant v_- . Classically, this constant ($v_- = v_2 - v_0$) is obtained by calculating the rates of the ZQ (v_0) and DQ (v_2) transitions using first-order perturbation theory. From this point of view, decomposing the product pv_- into the factors p and v_- is natural. The offset dependence of these two factors was visualized in fig. 5 (top row) and fig. 8 (middle row, black dashed lines). The curves for $B_1 = 6$ G and W band are reproduced on the left-hand side of fig. 10 (black and green lines).

1105

In contrast to this classical approach, here we considered the complete spin dynamics of relevance to the solid effect, including the dynamics of the coherences (fig. 2d), while the dynamics of three more operators, namely $S_n I_-$ ($n = x, y, z$), was included implicitly when we took the real part of $s_z i_{\pm}$. The remaining five operators which did not appear in our analysis were I_{\pm} and $S_n I_z$. The analysis was simplified by the realistic assumption that the electronic dynamics was not affected by

1110 the dipolar interaction with the nuclear spins. Thus, in our description, the purely electronic degrees of freedom constitute an isolated dynamical system, which influences the other dynamical variables but is not affected by them.

The main insight of our dynamical description of the solid effect relates to the role of the coherences. We demonstrated the involvement of two types of coherences: purely electronic and mixed electron-nuclear. Their evolution was described by two coupled Bloch equations. (This division of the complete dynamical system into a purely electronic part and the rest calls for a similar separation of the product pv_- in (64) into an electronic part and a mixed electron-nucleus part. Such factorization of pv_- is illustrated in the right half of fig. 10, where the purely electronic part is identified with the dispersive component of the EPR line. This would be the out-of-phase cw-EPR spectrum recorded under the same mw power as used in the DNP experiment. Then, from (56), the second factor is recognized to be $\delta^2 T_x$, where δ^2 accounts for the strength of the dipolar interaction (eq. (41)) and T_x takes care of the interconnections between the relevant electron-nucleus coherences at steady state (eq. (54)). The offset dependence of the dispersive EPR line was visualized before in fig. 5 (bottom row). The curve for $B_1 = 6$ G is reproduced on the right-hand side of fig. 2d), whose steady-state response was rationalized in terms of two band-pass filters connected in series (figs. 10 (blue line). The curve below it (orange line) corresponds to $\delta^2 T_x$ at W band, which is essentially the same as $\delta^2 T'_x$ that was shown in the second row of fig. ?? and 10)7 since at this high magnetic field T'_y contributes negligibly little.

1125 Because, as already illustrated above (fig. The involvement of the electron-nuclear coherences in the solid effect is directly manifested by the lines in the DNP field profile at the canonical offsets $\Omega \approx \pm \omega_I$. The involvement of the purely electronic coherences, on the other hand, is not directly visible, at least until one recognizes that the odd parity of the DNP field profile is a-9, middle row, W band), the classical approach and our new approach lead to the same product pv_- , the new factorization on the right-hand side of fig. 10 may appear as a purely mathematical exercise of little practical interest. Note, however, that recognizing the dispersive EPR line as contributing multiplicatively to the DNP enhancement suggests that the dispersive extrema could become visible in the field profile of ϵ_{SE} , provided that they are not fully suppressed by the factor $\delta^2 T_x$. Such possibility is completely missing in the classical description on the left-hand side of fig. 10, where any reference to the dispersive EPR line and its extrema is irrelevant.

1130 In Paper II we show that, in liquids, the random modulation of the dipolar interaction broadens the lines of the factor $\delta^2 T_x$ (fig. 10, orange line). When the tails of these broadened lines reach the extrema of the dispersive EPR line (blue line), the enhancement field profile exhibits features that are reminiscent of the DNP effect known as thermal mixing (Kuzhelev et al., 2022). These features are a direct manifestation of the dispersive EPR line, as intuited in the DNP spectrum (Sezer, 2023).

7.2 On the birth of the solid effect

1140 The issue of *Comptes rendus* from April 9, 1958, contained the article “Effect of nuclear polarization in liquids and gases adsorbed on charcoal” by Erb, Motchane and Uebersfeld (Erb et al., 1958a). It reported enhancements of the proton NMR signal of benzene upon mw irradiation of the EPR line of charcoal. The enhancements were positive at fields larger than the EPR resonance position and negative at smaller fields. Because fields symmetrically displaced from the resonance yielded the same magnification factor, the enhancement profile was odd in the field offset and resembled the dispersive component of the

EPR line. The similarity between the two prompted the authors to augment the Solomon equation (Solomon, 1955) with two new terms proportional to s_x and s_y (Erb et al., 1958a):

$$1145 \quad \dot{i}_z = \lambda(i_z - i_z^{\text{eq}}) + \mu(s_z - s_z^{\text{eq}}) + \nu s_x + \rho s_y. \quad (65)$$

Taking into account that “under saturation conditions $s_y = 0$ ” the authors arrived at

$$\dot{i}_z = \lambda(i_z - i_z^{\text{eq}}) + \mu(s_z - s_z^{\text{eq}}) + \nu s_x. \quad (66)$$

Assuming μ was small in their case, they solved (66) at steady state as

$$i_z^{\text{ss}} = i_z^{\text{eq}} - (\nu/\lambda)s_x, \quad (67)$$

1150 which explained the similarity between the field profile of the enhancement and the dispersive EPR line.

~~On a more quantitative level, we predicted that when the mw nutation frequency becomes comparable to the nuclear Larmor frequency, the optimal~~ Intriguingly, with $\mu = 0$, the phenomenological equation (65) is mathematically identical to (42), which expressed the time derivative of i_z at steady state as a linear combination of i_z , s_x and s_y . The argument of Erb et al. (1958a) that the contribution of s_y could be neglected, which led to (66), is justified by our analysis. Specifically, in 1155 the last row of fig. 7 we observed that the contribution of the absorptive component s_y to the rate constant ν_- was smaller than that of the dispersive component s_x . Moreover, we showed that the mathematically identical equation (55) was, in fact, exact within the framework of our treatment. Thus, the phenomenological equation (66) produces the correct steady state when its coefficients are selected as $\nu = -\delta^2 T_x$ and $\lambda = -\delta^2(T_i - T_i^0)$.

The next installment of *Comptes rendus* from April 14, 1958, contained Abragam and Proctor’s report “A new method for 1160 dynamic polarization of atomic nuclei in solids” (Abragam and Proctor, 1958), which was printed 132 pages after Erb et al. (1958a). This seminal contribution provided the modern theoretical understanding, and subsequently also the name, of the solid-state effect of dynamic nuclear polarization (DNP). In particular, the authors argued that the excitation of the forbidden transitions ~~should shift from the canonical solid effect positions to smaller offsets (fig. 8). Considering the high mw powers accessible in modern-day DNP spectrometers (Neudert et al., 2016), this observation should be relevant at S and X bands~~ (Neudert et al., 2017; Gizatullin et al., 2021). However, ~~$(++) \rightleftharpoons (--)$ and $(+-) \rightleftharpoons (-+)$, which become weakly allowed because the dipolar coupling yields mixed states of the form $(--)+q(-+)$, could be used for DNP. (\pm are the states of the two spin types, both taken as 1/2 for simplicity.) As an experimental verification of the theoretical proposal, the Boltzmann polarization of ^{19}F nuclei was used to enhance the NMR signal of ^6Li in a LiF monocrystal, thus demonstrating polarization transfer from nuclei with larger to nuclei with smaller gyromagnetic ratios (i.e., a nuclear solid effect).~~

1170 One month and a half after Abragam and Proctor’s report, in the May 28, 1958 issue of *Comptes rendus*, Erb, Motchane and Uebersfeld published another report with the lengthy title “On a new method of nuclear polarization in fluids adsorbed on charcoal. Extension to solids and in particular to irradiated organic substances” (Erb et al., 1958b). There, the authors state (our translation)

1175 The experiments [Erb et al. (1958a)] had been carried out with charcoal whose half-linewidth was 5 gauss and the multiplication factor seemed to reproduce the paramagnetic dispersion curve.

The new experiments [...] indicated that the increase in polarization of the proton in the adsorbed fluid is maximum in all cases, when the electronic and nuclear frequencies are chosen such that the nuclear resonance field differs from the electron resonance field $\delta H = \pm 5$ gauss (within 10%).

1180 These results support the suggestion of Abragam that the new theory of Abragam and Proctor on the nuclear polarization in solids (Abragam and Proctor, 1958) must apply to these new phenomena, and invalidates the interpretation proposed previously (Erb et al., 1958a).

The value of 5 gauss found in the case of the proton indeed corresponds to the value deduced from the theoretical formula $H_0 \pm \delta H = (\omega \pm \omega_N) / \gamma_e, \dots$

1185 This seems to have sealed the fate of the insightful observation of Erb et al. (1958a) that the odd parity of the solid-effect DNP field profile resembles the dispersive component of the EPR line.

With the understanding developed in the 65 years since these first publications on the solid effect, the additional transverse terms in (65) appear strange, and even disturbing. Nevertheless, our analysis showed that in one specific regime—steady state—equation (65) is exact. Admittedly, because of the ~~additional multiplication by the electronic polarization factor (fig. algebraic relationships between all dynamical variables at steady state, the transverse components in (65) can be expressed in terms~~ of the longitudinal component, as we did when going from (42) to (43). Such mathematical manipulation, however, only highlights the fact that the value of any description of spin dynamics by rate equations, independently of whether it contains transverse components or not, lies in the proper selection of the phenomenological rate constants. In this paper, we departed from the classical approach of identifying these rate constants with the transition probabilities per unit time. Instead, completely disregarding the dynamical aspect of the rate equations, we selected the phenomenological rate constants by requiring that the steady state of the exact quantum dynamics is correctly reproduced.

1195 By writing the rate equation of the nuclear polarization with explicit dispersive component (eq. 5, top row), the maxima of the enhancement end up in the vicinity of the canonical offsets even when the condition $\omega_1 \ll \omega_I$ is violated ((66)), Erb et al. (1958a) reached the conclusion that the DNP enhancement depends *multiplicatively* on s_x (eq. (67)). This conclusion is confirmed by our analysis. Indeed, from the new perspective illustrated on the right-hand side of fig. 9, last row, X band)-10, the DNP field profile acquires its odd parity in Ω directly from the dispersive component of the EPR line (blue line), exactly as intuited by Erb et al. (1958a). Certainly, one could explain the odd parity of the solid-effect DNP enhancement in various other ways that do not involve the dispersive EPR line, as has been done in the past 65 years. The validity of these other explanations, however, does not invalidate the intuition of Erb, Motchane, and Uebersfeld.

7.3 Conclusion

1205 In this paper we developed a novel way of thinking about the solid effect, which was grounded in the dynamics of the spins at steady state. The main insight of our dynamical description relates to the role of the coherences.

1210 While our analysis focused on the solid effect and the Hamiltonian (29), the systematic procedure for deriving the relevant equations of motion under a given spin Hamiltonian (Sec. 3.1), and the developed graphical representations to visualize the interplay of these equations (Sec. 4) and their steady state (Sec. 5), should be applicable to other related effects with different Hamiltonians.

The classical explanation of the solid effect in terms of ~~level-state~~ mixing (Abragam and Proctor, 1958) is static in nature and is thus hard to generalize to liquids where the dipolar interaction fluctuates randomly due to molecular motions. The time-dependent description of the solid effect ~~that we developed in the current paper~~ developed here naturally accommodates such stochastic modulation of the parameters of the Hamiltonian, in a way similar to the treatment of relaxation in liquids
1215 ~~(Abragam, 1961)~~ (Abragam, 1961, Ch. VIII). In the companion paper ~~we extend the formalism~~ (Sezer, 2023), the formalism is extended to the solid effect in liquids, and ~~validate its predictions~~ its predictions are validated against recent DNP experiments at J band (Kuzhelev et al., 2022).

Appendix A: Additional figures

1220 The numerical examples in the paper were for the excessively high mw field of $B_1 = 6$ G, which is reachable with a custom-designed resonance structure (Denysenkov et al., 2022). As the modern-day DNP experiments in solids are generally performed without a mw resonator, here we show numerical examples for the lower fields of $B_1 = 3$ G and $B_1 = 1$ G. Although these are still likely an order of magnitude larger than what is used in practice, the figures aim to illustrate how some of the features discussed in the paper progressively change upon reduction of B_1 .

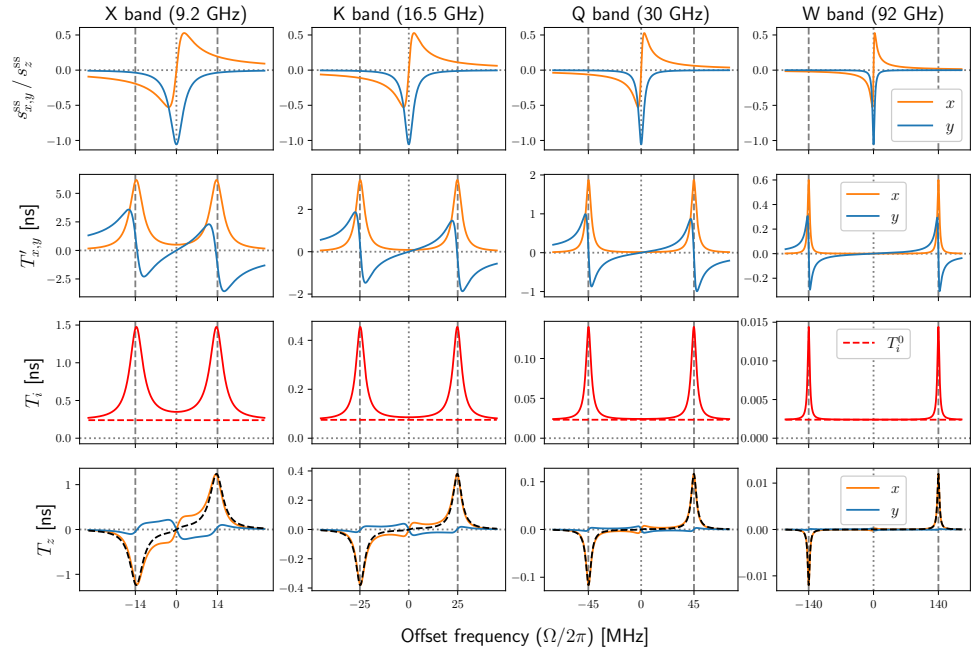
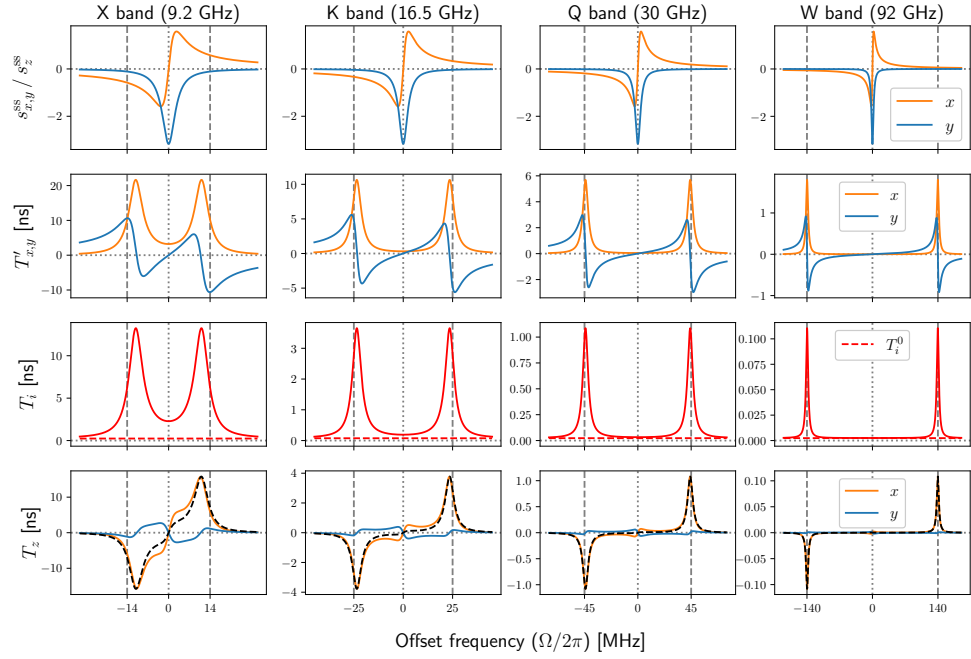


Figure A1. Same as fig. 22-7 with smaller mw fields of $B_1 = 3$ G (top) and $B_1 = 1$ G (bottom).

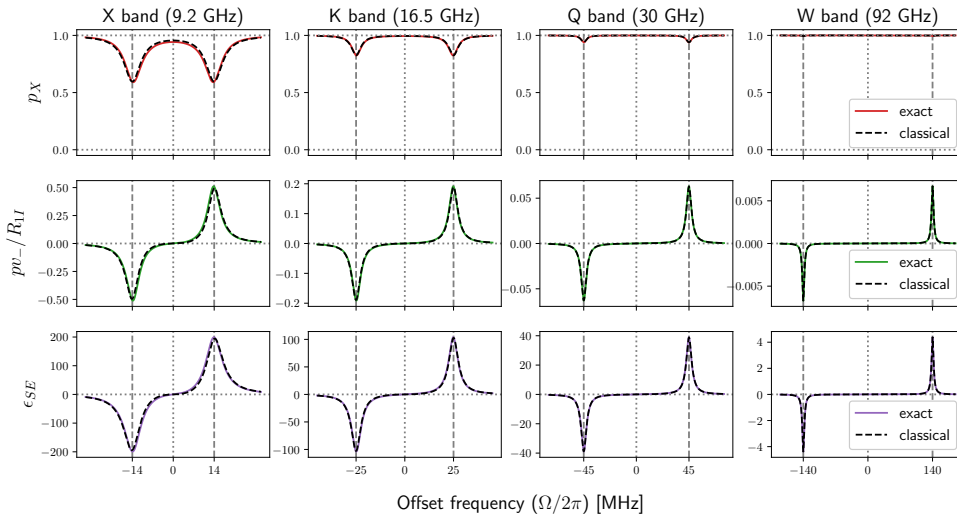
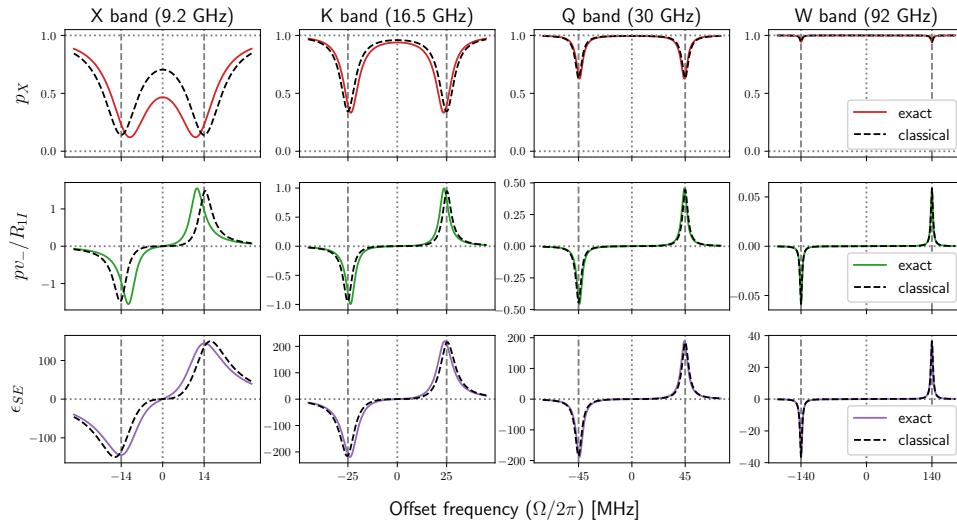


Figure A2. Same as fig. 9 with smaller mw fields of $B_1 = 3$ G (top) and $B_1 = 1$ G (bottom).

Author contributions. DS developed the theory and wrote the paper.

1225 *Competing interests.* No competing interests are present.

Acknowledgements. Thomas Prisner is gratefully acknowledged for providing the scientific environment that enabled the reported research. Numerous discussions with Thomas Prisner, Andriy Marko, Vasyl Denysenkov, Andrei Kuzhelev, and Danhua Dai were instrumental in developing the presented ideas. Funding was provided by the German Research Foundation (DFG grant 405972957).

References

- 1230 Abragam, A.: Overhauser Effect in Nonmetals, *Physical Review*, 98, 1729–1735, <https://doi.org/10.1103/PhysRev.98.1729>, 1955.
Abragam, A.: *The Principles of Nuclear Magnetism*, Oxford University Press, New York, 1961.
Abragam, A. and Goldman, M.: Principles of dynamic nuclear polarisation, 41, 395, <https://doi.org/10.1088/0034-4885/41/3/002>, 1978.
Abragam, A. and Proctor, W. G.: Une nouvelle méthode de polarisation dynamique des noyaux atomiques dans les solides, *Compt. rend.*, 246, 2253–2256, 1958.
- 1235 Barker, W. A.: Dynamic Nuclear Polarization, *Reviews of Modern Physics*, 34, 173–185, <https://doi.org/10.1103/RevModPhys.34.173>, 1962.
Bengs, C. and Levitt, M. H.: SpinDynamica: Symbolic and numerical magnetic resonance in a Mathematica environment, *Magnetic Resonance in Chemistry*, 56, 374–414, <https://doi.org/https://doi.org/10.1002/mrc.4642>, 2018.
Can, T. V., Walsh, J. J., Swager, T. M., and Griffin, R. G.: Time domain DNP with the NOVEL sequence, *The Journal of Chemical Physics*, 143, 054201, <https://doi.org/10.1063/1.4927087>, 2015.
- 1240 Carver, T. R. and Slichter, C. P.: Polarization of Nuclear Spins in Metals, *Physical Review*, 92, 212–213, <https://doi.org/10.1103/PhysRev.92.212.2>, 1953.
Carver, T. R. and Slichter, C. P.: Experimental Verification of the Overhauser Nuclear Polarization Effect, *Physical Review*, 102, 975–980, <https://doi.org/10.1103/PhysRev.102.975>, 1956.
Cohen-Tannoudji, C., Diu, B., and Laloë, F.: *Quantum Mechanics*, vol. 2, Wiley-VCH, 2nd edn., 2019.
- 1245 Denysenkov, V., Dai, D., and Prisner, T. F.: A triple resonance (e , $1H$, ^{13}C) probehead for liquid-state DNP experiments at 9.4 Tesla, *Journal of Magnetic Resonance*, 337, 107185, <https://doi.org/https://doi.org/10.1016/j.jmr.2022.107185>, 2022.
Duijvestijn, M. J., Wind, R. A., and Smidt, J.: A quantitative investigation of the dynamic nuclear polarization effect by fixed paramagnetic centra of abundant and rare spins in solids at room temperature, *Physica B+C*, 138, 147–170, [https://doi.org/https://doi.org/10.1016/0378-4363\(86\)90503-6](https://doi.org/https://doi.org/10.1016/0378-4363(86)90503-6), 1986.
- 1250 Erb, E., Motchane, J.-L., and Uebersfeld, J.: Effet de polarisation nucléaire dans les liquides et les gaz adsorbés sur les charbons, *Compt. rend.*, 246, 2121–2123, 1958a.
Erb, E., Motchane, J.-L., and Uebersfeld, J.: Sur une nouvelle méthode de polarisation nucléaire dans les fluides adsorbés sur les charbons. extension aux solides et en particulier aux substances organiques irradiées., *Compt. rend.*, 246, 3050–3052, 1958b.
Gizatullin, B., Mattea, C., and Stapf, S.: Molecular Dynamics in Ionic Liquid/Radical Systems, *The Journal of Physical Chemistry B*, 125, 4850–4862, <https://doi.org/10.1021/acs.jpcc.1c02118>, 2021.
Gizatullin, B., Mattea, C., and Stapf, S.: Three mechanisms of room temperature dynamic nuclear polarization occur simultaneously in an ionic liquid, *Physical Chemistry Chemical Physics*, 24, 27004–27008, <https://doi.org/10.1039/D2CP03437A>, 2022.
- Henstra, A. and Wenckebach, W. T.: The theory of nuclear orientation via electron spin locking (NOVEL), *Molecular Physics*, 106, 859–871, <https://doi.org/10.1080/00268970801998262>, 2008.
- 1260 Henstra, A., Dirksen, P., Schmidt, J., and Wenckebach, W. T.: Nuclear spin orientation via electron spin locking (NOVEL), *Journal of Magnetic Resonance* (1969), 77, 389–393, [https://doi.org/https://doi.org/10.1016/0022-2364\(88\)90190-4](https://doi.org/https://doi.org/10.1016/0022-2364(88)90190-4), 1988.
Hovav, Y., Feintuch, A., and Vega, S.: Dynamic nuclear polarization assisted spin diffusion for the solid effect case, *The Journal of Chemical Physics*, 134, 074509, <https://doi.org/10.1063/1.3526486>, 2011.
Jain, S. K., Mathies, G., and Griffin, R. G.: Off-resonance NOVEL, *The Journal of Chemical Physics*, 147, 164201, <https://doi.org/10.1063/1.5000528>, 2017.

- Keeler, J.: *Understanding NMR Spectroscopy*, Wiley, 2nd edn., 2010.
- Kuzhelev, A. A., Dai, D., Denysenkov, V., and Prisner, T. F.: Solid-like Dynamic Nuclear Polarization Observed in the Fluid Phase of Lipid Bilayers at 9.4 T, *Journal of the American Chemical Society*, 144, 1164–1168, <https://doi.org/10.1021/jacs.1c12837>, 2022.
- 1270 Leblond, J., Uebbersfeld, J., and Korrinda, J.: Study of the Liquid-State Dynamics by Means of Magnetic Resonance and Dynamic Polarization, *Physical Review A*, 4, 1532–1539, <https://doi.org/10.1103/PhysRevA.4.1532>, 1971.
- Neudert, O., Mattea, C., and Stapf, S.: A compact X-Band resonator for DNP-enhanced Fast-Field-Cycling NMR, *Journal of Magnetic Resonance*, 271, 7–14, <https://doi.org/https://doi.org/10.1016/j.jmr.2016.08.002>, 2016.
- Neudert, O., Mattea, C., and Stapf, S.: Molecular dynamics-based selectivity for Fast-Field-Cycling relaxometry by Overhauser and solid effect dynamic nuclear polarization, *Journal of Magnetic Resonance*, 276, 113–121, <https://doi.org/https://doi.org/10.1016/j.jmr.2017.01.013>, 2017.
- 1275 Overhauser, A. W.: Polarization of Nuclei in Metals, *Physical Review*, 92, 411–415, <https://doi.org/10.1103/PhysRev.92.411>, 1953.
- Pinon, A. C.: *Spin Diffusion in Dynamic Nuclear Polarization Nuclear Magnetic Resonance*, Ph.D. thesis, EPFL, 2018.
- Quan, Y., Steiner, J., Ouyang, Y., Tan, K. O., Wenckebach, W. T., Hautle, P., and Griffin, R. G.: Integrated, Stretched, and Adiabatic Solid Effects, *The Journal of Physical Chemistry Letters*, 13, 5751–5757, <https://doi.org/10.1021/acs.jpcclett.2c01147>, 2022.
- 1280 Quan, Y., Ouyang, Y., Mardini, M., Palani, R. S., Banks, D., Kempf, J., Wenckebach, W. T., and Griffin, R. G.: Resonant Mixing Dynamic Nuclear Polarization, [10.26434/chemrxiv-2023-h106f](https://doi.org/10.26434/chemrxiv-2023-h106f), 2023.
- Sezer, D.: The solid-state DNP effect in liquids, *Magnetic Resonance* (accepted), <https://doi.org/https://doi.org/10.5194/mr-2023-2>, 2023.
- Shankar, R.: *Principles of Quantum Mechanics*, Springer, 2nd edn., 1994.
- Shankar Palani, R., Mardini, M., Quan, Y., and Griffin, R. G.: Dynamic nuclear polarization with trityl radicals, *Journal of Magnetic Resonance*, 349, 107 411, <https://doi.org/https://doi.org/10.1016/j.jmr.2023.107411>, 2023.
- 1285 Smith, A. A., Corzilius, B., Barnes, A. B., Maly, T., and Griffin, R. G.: Solid effect dynamic nuclear polarization and polarization pathways, *The Journal of Chemical Physics*, 136, 015 101, <https://doi.org/10.1063/1.3670019>, 2012.
- Solomon, I.: Relaxation Processes in a System of Two Spins, *Phys. Rev.*, 99, 559–565, 1955.
- Van Kampen, N. G.: Elimination of fast variables, *Physics Reports*, 124, 69–160, [https://doi.org/https://doi.org/10.1016/0370-1573\(85\)90002-X](https://doi.org/https://doi.org/10.1016/0370-1573(85)90002-X), 1985.
- 1290 Webb, R. H.: Steady-State Nuclear Polarizations via Electronic Transitions, *American Journal of Physics*, 29, 428–444, <https://doi.org/10.1119/1.1986008>, 1961.
- Wenckebach, T.: *Essentials of Dynamic Nuclear Polarization*, Spindrift Publications, The Netherlands, 2016.
- Wind, R. A., Duijvestijn, M. J., van der Lugt, C., Manenschijn, A., and Vriend, J.: Applications of dynamic nuclear polarization in ¹³C NMR in solids, *Progress in Nuclear Magnetic Resonance Spectroscopy*, 17, 33–67, [https://doi.org/https://doi.org/10.1016/0079-6565\(85\)80005-4](https://doi.org/https://doi.org/10.1016/0079-6565(85)80005-4), 1985.
- 1295 Yang, C., Ooi Tan, K., and Griffin, R. G.: DNPSOUP: A simulation software package for dynamic nuclear polarization, *Journal of Magnetic Resonance*, 334, 107 107, <https://doi.org/https://doi.org/10.1016/j.jmr.2021.107107>, 2022.